nature communications

Article

https://doi.org/10.1038/s41467-025-56853-3

Human and mouse proteomics reveals the shared pathways in Alzheimer's disease and delayed protein turnover in the amyloidome

Received: 22 October 2024

Accepted: 4 February 2025

Published online: 11 February 2025

Check for updates

Jay M. Yarbro[1,2,11], Xian Han[1,2,11], Abhijit Dasgupta[1,2,10,11], Ka Yang[1,2,11], Danting Liu[1,2], Him K. Shrestha[1,2], Masihuz Zaman[1,2], Zhen Wang[1,2], Kaiwen Yu[3], Dong Geun Lee[1,2], David Vanderwall[1,2], Mingming Niu[1,2], Huan Sun[1,2], Boer Xie[3], Ping-Chung Chen[1,2], Yun Jiao[1,2], Xue Zhang[1,2], Zhiping Wu[1,2], Surendhar R. Chepyala[1,2], Yingxue Fu[3], Yuxin Li[3], Zuo-Fei Yuan[3], Xusheng Wang[4], Suresh Poudel[3], Barbora Vagnerova[5], Qianying He[5], Andrew Tang[5], Patrick T. Ronaldson[5], Rui Chang[5], Gang Yu[6], Yansheng Liu[7,8,9] & Junmin Peng[1,2,3]

Murine models of Alzheimer's disease (AD) are crucial for elucidating disease mechanisms but have limitations in fully representing AD molecular complexities. Here we present the comprehensive, age-dependent brain proteome and phosphoproteome across multiple mouse models of amyloidosis. We identified shared pathways by integrating with human metadata and prioritized components by multi-omics analysis. Collectively, two commonly used models (5xFAD and APP-KI) replicate 30% of the human protein alterations; additional genetic incorporation of tau and splicing pathologies increases this similarity to 42%. We dissected the proteome-transcriptome inconsistency in AD and 5xFAD mouse brains, revealing that inconsistent proteins are enriched within amyloid plaque microenvironment (amyloidome). Our analysis of the 5xFAD proteome turnover demonstrates that amyloid formation delays the degradation of amyloidome components, including Aβ-binding proteins and autophagy/lysosomal proteins. Our proteomic strategy defines shared AD pathways, identifies potential targets, and underscores that protein turnover contributes to proteome-transcriptome discrepancies during AD progression.

Alzheimer's disease (AD), a progressive neurodegenerative disorder, is the most common cause of dementia, affecting more than 6 million Americans[1]. AD pathology initiates decades before the onset of gross behavioral symptoms and is primarily defined by the aggregation of β-amyloid peptide (Aβ) in extracellular plaques and of hyperphosphorylated tau proteins as intracellular neurofibrillary tangles[2–4]. In addition to Aβ and tau, other coexisting molecular changes[4,5], such as α-synuclein[6,7], TDP-43[5,8], and U1 snRNP[9,10], may play important roles in

[1]Department of Structural Biology, St. Jude Children's Research Hospital, Memphis, TN, USA. [2]Department of Developmental Neurobiology, St. Jude Children's Research Hospital, Memphis, TN, USA. [3]Center for Proteomics and Metabolomics, St. Jude Children's Research Hospital, Memphis, TN, USA. [4]Department of Neurology, University of Tennessee Health Science Center, Memphis, TN, USA. [5]Department of Pharmacology, College of Medicine, University of Arizona, Tucson, AZ, USA. [6]Department of Neuroscience, Peter O'Donnell Jr. Brain Institute, University of Texas Southwestern Medical Center, Dallas, TX, USA. [7]Department of Pharmacology, Yale University School of Medicine, New Haven, CT, USA. [8]Yale Cancer Biology Institute, Yale University School of Medicine, West Haven, CT, USA. [9]Department of Biomedical Informatics & Data Science, Yale University School of Medicine, West Haven, CT, USA. [10]Present address: Department of Computer Science and Engineering, SRM University AP, Andhra Pradesh, India. [11]These authors contributed equally: Jay M. Yarbro, Xian Han, Abhijit Dasgupta, Ka Yang. e-mail: Junmin.peng@stjude.org

disease progression. Genetic analyses of AD and control cases have elucidated three causative genes (*APP*, *PSEN1*, and *PSEN2*), high-risk genes (*APOE4* and *TREM2*) and about 100 low-risk genes and loci[11–20]. However, the molecular mechanisms of these proteins/genes in AD development are not fully understood, often due to the lack of suitable cellular or animal models.

More than 100 genetic AD mouse models have been developed[21–24], predominantly by mimicking genetic mutations linked to familial AD, such as the lines of 5xFAD[25,26], 3xTG[27], and APP-KI including APP^{NLF} (NLF) and APP^{NLGF} (NLGF)[28]. However, none of these models capture the full spectrum of AD molecular events and pathologies as they exhibit less severe neurodegeneration compared to human patients. Ideally, researchers should fully understand the advantages and limitations of mouse models to select the most appropriate one for addressing specific hypotheses; however, no comprehensive resources are currently available.

Rapid developments in omics technologies provide an opportunity of thoroughly evaluating disease models on a global scale and exploring their relevance by comparisons with human data[29–31]. Transcriptomic analyses of the amyloidosis mouse models revealed changes in expression of genes linked to immune response, synaptic function, and neuronal signaling[32–34]. However, RNA levels do not always align with protein levels due to posttranscriptional processes, such as translation and protein turnover[35]. Indeed, notable inconsistencies between transcript and protein levels in AD and 5xFAD mice were observed[36,37]. Complementary proteomic studies in AD mice[38–41] not only corroborated transcriptomic findings, but also identified RNA-independent protein alterations[36,39,42] and changes in protein turnover[43,44]. These early proteomic studies in the AD mice uncovered some molecular changes but they were often limited by inadequate proteomic depth, restricted analysis of individual mouse models, and/or insufficient comparison with human AD datasets.

Here we present a deep, age-dependent analysis of 10,369 proteins (10,331 genes) and 12,096 phosphopeptides (10,532 phosphosites) across commonly used AD models: 5xFAD[25], NLF[28], and NLGF[28]. We also profiled two additional AD models (3xTG[27] and BiG[45]), performed human-mouse comparisons, and analyzed transcriptome-proteome inconsistency in both mouse and human. To explore the contribution of protein degradation to the transcriptome-proteome inconsistency, we measured the turnover rates of 8492 brain proteins and found that amyloid formation delays the degradation of amyloidome components. Thus, our comprehensive proteomic analysis identifies shared AD pathways and demonstrates altered protein turnover in amyloid plaques in AD mice. All data are freely available and searchable through an interactive website.

Results

Proteome profiling of multiple AD amyloidosis models reveals shared pathways

We compared proteomic readout of three mouse models of amyloidosis at different ages, with early and late symptoms (Fig. 1a, Supplementary Data 1): (i) 5xFAD (3-, 6-, 12-month-old), overexpressing human *APP* and *PSEN1* genes carrying a total of five human disease mutations under the *Thy1* promoter, which promotes rapid onset of amyloid pathology[25]; (ii) NLF (3-, 12-month-old, with weak pathology) and NLGF (3-, 6-, 12-, 18-month-old, with strong pathology), both being next-generation knock-in models with humanized Aβ without gene overexpression[28]. We also analyzed age-matched wild type (WT) control mice for each mouse line.

Using our optimized tandem mass tag (TMT) method, coupled with extensive two-dimensional liquid chromatography (LC/LC) and high-resolution tandem mass spectrometry (MS/MS, Supplementary Fig. 1a)[46–49], we profiled a total of 66 mouse brains (cortex) in multiple TMT batches with deep proteome coverage (Supplementary Data 2), identified more than 900,000 peptide-spectrum matches (PSMs), ~330,000 peptides, and 10,369 unique proteins (10,331 genes) that were shared in all animals, with a protein false discovery rate (FDR) below 0.01 (Fig. 1b, Supplementary Data 3). After protein quantification based on TMT reporter ions, sample loading bias was corrected as shown in a box plot (Supplementary Fig. 1b), and the batch effect was normalized and confirmed by PCA analysis (Supplementary Fig. 1c). As expected, the Aβ tryptic peptide (R.HDSGYEVHHQK.L) shows age-dependent increases in all AD mice, with higher levels in 5xFAD and NLGF than NLF, consistent with the reported pathologies in these mice (Fig. 1c, Supplementary Data 4).

We examined the effect of aging using only WT mice (3-, 6-, 12-, 18-month-old) to avoid the confounding impact of Aβ insult in different genotypes. When comparing 3-month-old mice to any other aged mice, differential expression (DE) analysis identified 183 age-dependent proteins [FDR < 0.05, $|\log_2$Fold Change (FC)| > two standard deviations (SD)], with 129 proteins upregulated and 54 proteins downregulated with age (Supplementary Fig. 2a). These age-dependent proteins are predominantly associated with processes such as extracellular matrix remodeling, lysosomal activity, and synaptic signaling (Supplementary Data 5). The upregulated proteins are enriched in the Gene Ontology (GO)[50] terms of collagen-containing extracellular matrix, perineuronal net, lysosome, glutathione metabolic process, etc. (Supplementary Fig. 2b). Conversely, the downregulated proteins are enriched in cell periphery, cell junction, and neuronal components, including synapse, axon, dendritic spine, etc. (Supplementary Fig. 2c, Supplementary Data 6).

We then performed DE analysis at different ages for each genotype using WT controls (FDR < 0.05, $|\log_2$FC | > 2 SD, Supplementary Data 7), excluding human Aβ peptide as it is not present in the WT mice. NLF exhibits a few DE proteins (DEPs), in agreement with its weak pathology[51] (Fig. 1d). In contrast, the 5xFAD and NLGF models demonstrate significant protein alterations, which increased with age for both models (Fig. 1d). For instance, a volcano curve shows 605 DEPs in 12-month-old NLGF mice compared to the WT (Fig. 1e), reflecting its strong amyloid phenotype[25,28]. When summing the DEPs at different ages, there are 1382 DEPs in 5xFAD, only 7 in NLF and 1142 in NLGF. Moreover, we found that the numbers of DEPs are highly correlated with the Aβ accumulation across all tested models ($R = 0.86$, Supplementary Data 8).

In spite of the genetic difference between 5xFAD and NLGF models[21,28], we observed comparable proteomic signatures in the two models. Among 1914 total DEPs in 5xFAD and NLGF, 610 (32%) overlap, of which 98% (597/610) exhibit consistent directional changes (either upregulated or downregulated). The remaining DEPs, 772 (40%) in 5xFAD and 532 (28%) in NLGF, are genotype-specific, but show a similar age-dependent trend in both AD models (Fig. 1f). Differences appear primarily driven by statistical thresholding rather than distinct biology. Overall, the proteomic profiles of 5xFAD and NLGF exhibit broadly similar patterns.

We performed Gene Ontology analysis on the 597 overlapping DEPs and found enrichment in extracellular matrix, lysosome/endocytosis, immune response, synaptic signaling, and binding to Aβ, integrin, lipid, calcium ion, etc. (Fig. 1g, Supplementary Data 9). The overlapping DEPs were mapped to protein-protein interaction (PPI) networks, revealing significant interacting modules of immune response, complement, lipid metabolism, proteolysis/autophagy, and an amyloid-binding extracellular matrix protein network (amyloid matrisome)[37] (Fig. 1h). These findings suggest that proteins and pathways shared between 5xFAD and NLGF are critical for amyloidosis pathogenesis and immune response, consistent with previous reports in human AD[36,37,52].

Phosphoproteome profiling of AD models highlights alterations independent of protein levels

Since protein phosphorylation is known to contribute to AD pathogenesis[53,54], we profiled the phosphoproteome in the same set of

https://doi.org/10.1038/s41467-025-56853-3

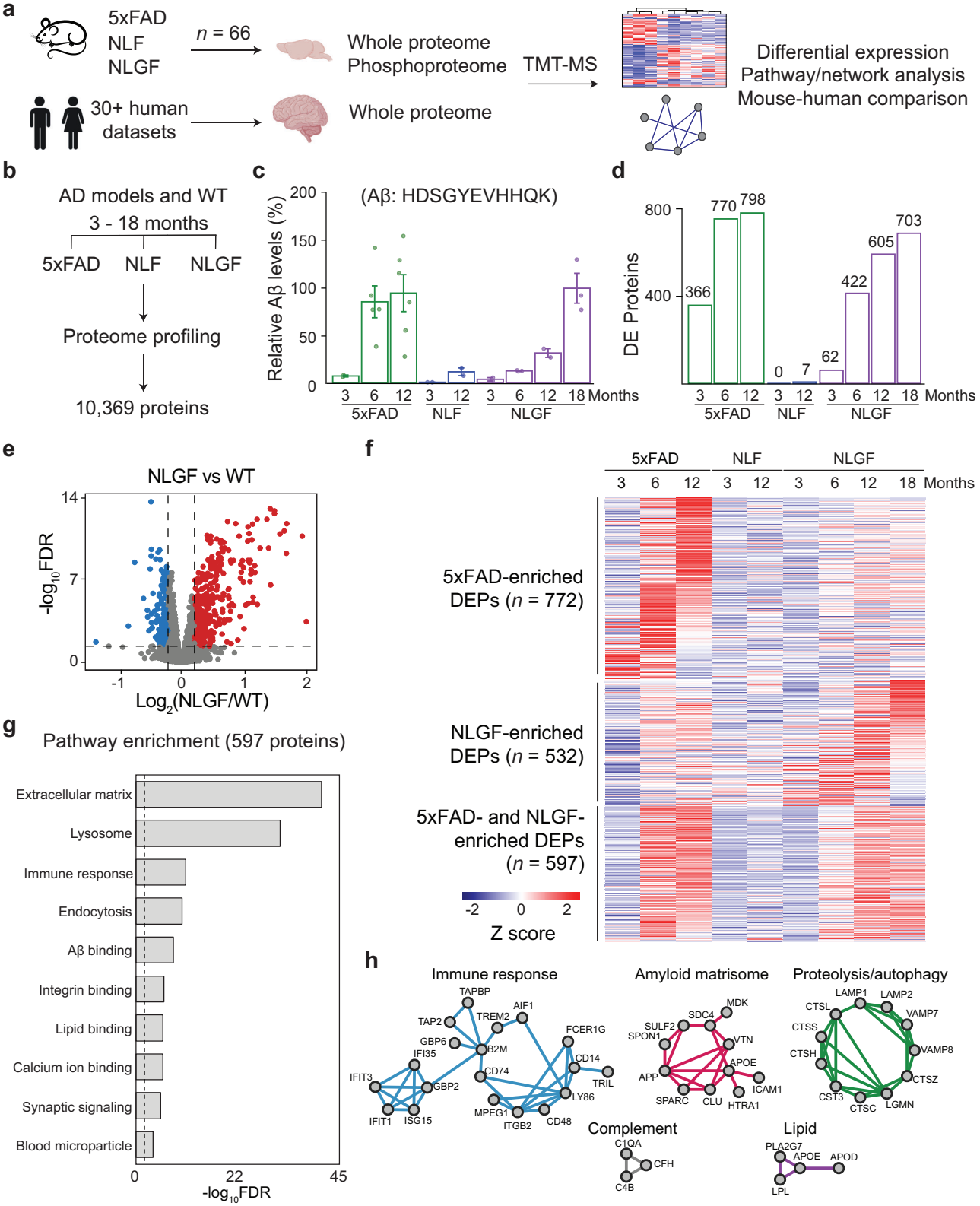

NLGF (3-, 6-, 12-, 18-month-old) mice and 5xFAD (12-month-old) and their age-matched WT controls. We used 5xFAD mice at a single age as a validation model following comprehensive discovery profiling of the age-dependent phosphoproteome in NLGF mice. The profiling was also performed using the TMT-LC/LC-MS/MS method[46–49], with an additional step of phosphopeptide enrichment to improve the phosphoproteome coverage[55] (Supplementary Fig. 3a-c). When combining phosphoproteome data from all TMT batches, we quantified 129,906 unique phosphopeptides (82,261 phosphosites on 10,502 proteins, peptide FDR < 0.01, Supplementary Data 10). Because of the incomplete coverage of phosphoproteome in individual TMT batches, the overlap between different TMT batches is often low[56]. When we extracted the phosphopeptides shared in all 36 mice, the number dropped to 12,096 phosphopeptides (10,532 phosphosites on 2814

https://doi.org/10.1038/s41467-025-56853-3

Fig. 1 | Brain MS analysis reveals proteomic changes that are shared in AD mouse models. a Schematic plan of this study. Mouse cortical tissues from AD models of amyloidosis (5xFAD, NLF, NLGF, and matched WT, total $n = 66$ for 16 conditions, averaged $n = \sim 4$ per condition) were analyzed by TMT-LC/LC-MS/MS and compared with human metadata. **b** Proteins quantified at different ages (3-18 months). **c** Aβ levels quantified by MS using the peptide HDSGYEVHHQK (Average value ± SD, $n = 2, 5, 6, 2, 2, 2, 3, 2, 3$, for each group, left to right). The values were averaged for each age and model, then normalized to 12-month-old 5xFAD (100%). **d** DEPs between AD mice and WT controls at increasing ages, defined by moderated *t*-test with statistical cutoffs (FDR < 0.05, |log2FC| > 2 SD). **e** Representative volcano plot for NLGF-WT comparison (moderated *t*-test). Individual proteins correspond to data points and are color coded red or blue if up- or down-regulated as defined by statistical cutoffs, respectively (FDR < 0.05, |log2FC| > 2 SD, dashed lines). **f** Heatmap of DEPs identified in AD mice at any age or genotype, including the proteins enriched in 5xFAD or NLGF and those shared by both mice. **g** Pathway analysis of shared DEPs in 5xFAD and NLGF. FDR was derived from *p* values (Fisher's exact test) by the Benjamini-Hochberg procedure. **h**, Enriched PPI modules from biological processes using the shared DEPs. Brain images created in BioRender. Yarbro, J. (2025) https://BioRender.com/a05v379.

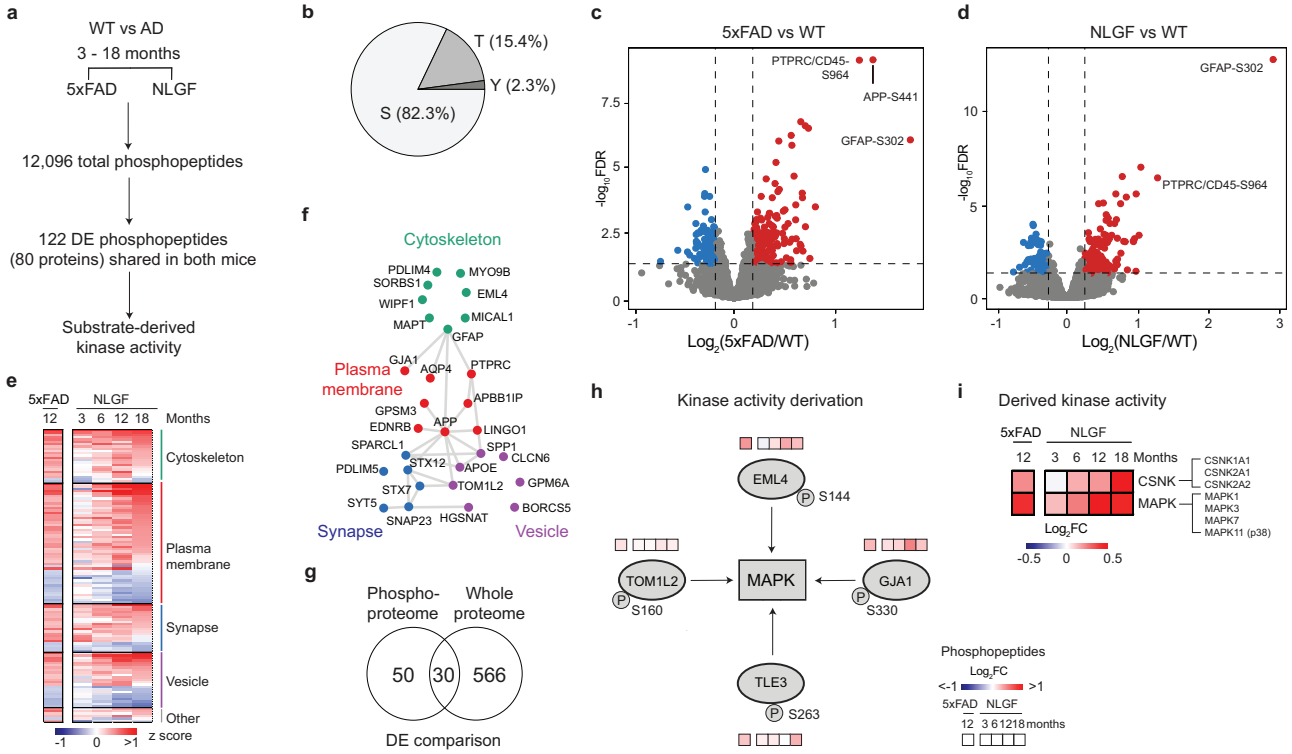

Fig. 2 | Tissue phosphoproteomics defines a new layer of regulation beyond whole proteome. a Phosphoproteome profiling was performed across 36 5xFAD and NLGF mice and their age-matched controls. We quantified 12,096 phosphopeptides (peptide FDR < 0.01) shared in all mice and performed statistical comparisons by moderated *t*-test. 122 DE phosphopeptides (80 proteins) were identified (FDR < 0.05, $|\log_2 FC| > 2$ SD). **b** Distribution of phospho-Ser/Thr/Tyr in identified phosphosites. **c** Volcano plot of phosphoproteome data for 12-month-old 5xFAD compared to WT. Dashed lines indicate cutoffs. **d** Volcano plot of phosphoproteome data for 12-month-old NLGF compared to WT. **e** Heatmap of DE phosphoproteins in 5xFAD and NLGF mice, with protein subcellular location shown. **f** PPI modules of DE phosphoproteins. **g** The overlap of DEPs in phosphoproteomics and whole proteome analysis. Only consistent DEPs in both AD models were counted. **h** Bioinformatics method for identifying altered kinase activities. Kinase-substrate linkages were extracted to infer kinase activities by the KSEA algorithm. An example of MAPK activation is based on KSEA. Phosphopeptide levels are displayed using the accompanying gradients. **i** Heatmap of derived kinase activities. The fold change of 5xFAD and NLGF was calculated by comparison with WT.

proteins, Fig. 2a, Supplementary Data 11). These shared phosphopeptides contain 8665 pS (82.3%), 1625 pT (15.4%), and 242 pY (2.3%) sites (Fig. 2b), similar to the site distribution in other large phosphoproteome analyses[36,57].

We then carried out pairwise DE analysis using age-matched WT controls for both 5xFAD and NLGF mice, identifying 122 consistent DE phosphopeptides (80 DE phosphoproteins) in the two mouse models (FDR < 0.05, $|\log_2 FC| > 2$ SD, Supplementary Data 12). For example, in both mice, the phosphorylation levels of PTPRC/CD45 S964 and GFAP T299 are significantly increased, indicating the activation of microglia and astrocytes, respectively (Fig. 2c, d). The 80 DE phosphoproteins are enriched in several pathways and PPI networks of cytoskeleton, plasma membrane, synapse, and vesicle (Fig. 2e, 2f, Supplementary Data 13). These pathways are consistent with those revealed in phosphoproteomic studies of human AD[54,58].

Notably, only 30 (37.5%) of the 80 DE phosphoproteins showed significant changes at the proteome level (Fig. 2g), suggesting that the differences in phosphorylation are primarily due to altered kinase/phosphatase activity in the brain, independent of the protein levels. To quantify the change in kinase activities based on these DE phosphopeptides, we derived alterations in kinase families by the computer algorithm of kinase-substrate enrichment analysis (KSEA)[59]. For instance, the MAPK activity could be inferred from its DE substrates of TOM1L2, EML4, GJA1, and TLE3 (Fig. 2h). The analysis identified the upregulation of two kinase families: casein kinase (CSNK, $p = 0.031$) and mitogen-activated protein kinase (MAPK, including p38 kinase, $p = 3.65 \times 10^{-11}$) (Fig. 2i). Consistently, MAPK pathway deregulation was previously highlighted in several cohort studies of human AD[36,37,54]. Thus, our KSEA analysis suggests the deregulation of numerous kinases that are relevant to amyloid pathology.

https://doi.org/10.1038/s41467-025-56853-3

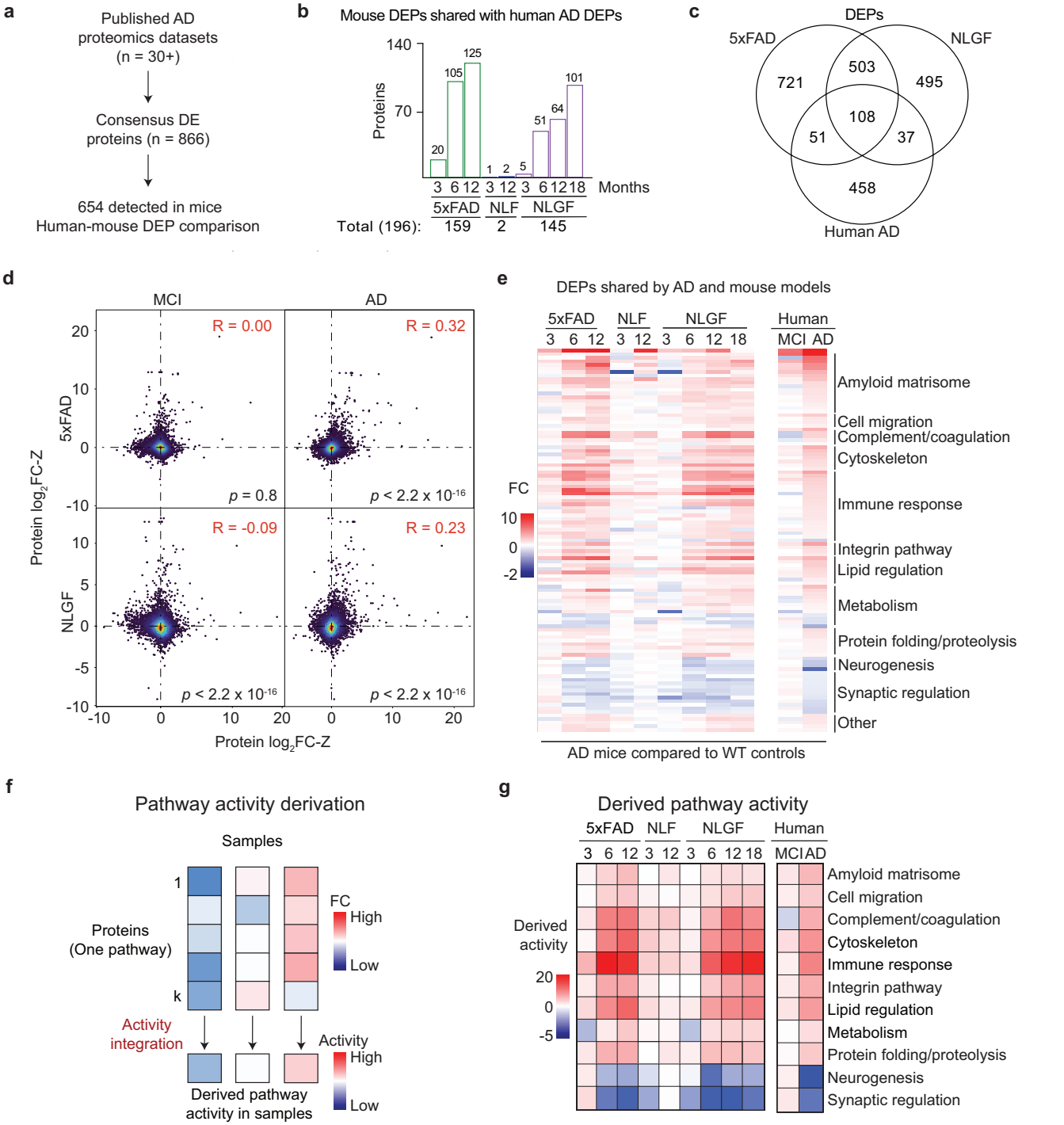

Fig. 3 | Comparison of mouse proteomics to human metadata identifies shared proteomic changes. a We identified 866 proteins that are consistently altered in more than 30 human AD proteomics studies, 654 of which were quantified in the proteomic analysis of the AD mice. Of these, 196 (30%) are differentially expressed in at least one mouse model (FDR < 0.05, $|\log_2 FC| > 2$ SD). **b** Number of overlapping DEPs between human AD and different mouse models. **c** DEPs shared by human AD, 5xFAD, and NLGF mice. **d** Scatter plot comparisons between Z scores of $\log_2$fold change values ($\log_2$FC-Z) of human AD/control cases and mouse models/WT at 12-month ages. Each dot represents one protein, and the color shows the dot density. Pearson correlation (R) values and associated p values are shown. **e** Heatmap showing $\log_2$FC values of human-mouse shared AD proteins, classified by biological pathways (moderated t-test, FDR < 0.05). **f** Workflow for deriving pathway activities. The FC of proteins in each pathway are integrated to calculate the pathway activity. **g** Heatmap of pathway activities in AD and mouse models.

Human-mouse comparison identifies shared AD pathways

To investigate the relevance of the mouse models, we compared the DEPs in 5xFAD and NLGF with human metadata[36,37,52,60]. We focused on 866 human DEPs that consistently exhibited significant changes in deep AD proteomics studies (Fig. 3a, Supplementary Data 14), for which 654 homologous proteins were detected by MS in mice. The sum of 5xFAD and NLGF DEPs corresponds to 30% (196/654) of the AD DEPs and demonstrates age-dependency (Fig. 3b). The three datasets share a core set of 108 DEPs (Fig. 3c). Further analysis reveals that 5xFAD and NLGF DEPs align more closely with late-stage AD ($R = 0.32$ and 0.23, respectively) than with mild cognitive impairment (MCI) ($R = 0.00$ and -0.09, respectively), although both correlations are

weak. This implies that these mouse models may be more representative of the amyloidosis in the advanced AD stages rather than that in the early, asymptomatic phase (Fig. 3d). Among the consistent core DEPs, approximately half exhibit cell-type specificity, with 42% specific to microglia, 29% to neurons, 25% to astrocytes, 2% to endothelial cells, and 2% to oligodendrocytes. These findings underscore the contributions of various cell types to disease development and highlight the prominent role of microglia.

We then examined the 108 DEPs consistent in both mouse models and human AD (Fig. 3e), and derived their pathway activities by integrating individual components with a mathematical formula[61,62] (Fig. 3f). Several pathway activities are upregulated, including amyloid matrisome, cell migration, complement and coagulation, cytoskeleton, immune response, integrin pathway, lipid regulation, metabolism and protein folding/proteolysis; two pathways—neurogenesis and synaptic regulation—are downregulated (Fig. 3g, Supplementary Data 14 and 15).

Additional pathologies beyond amyloidosis in mice increase similarity to AD

The 5xFAD and NLGF mouse models of amyloidosis fail to capture the entire spectrum of AD-related proteomic changes. This discrepancy may be attributed to the absence of other pathologies found in human AD, such as tauopathies[53] and splicing dysfunctions[9]. We further profiled two other AD mouse models with additional pathologies (Fig. 4a, Supplementary Fig. 4a-e, Supplementary Data 1): (i) 3xTG, displaying both amyloid plaque and tau tangle pathologies[27], and (ii) BiGenic (BiG) mice, generated by crossing 5xFAD with N40K transgenic mice recapitulating both amyloid pathology and the newly discovered U1 snRNP splicing dysfunction in AD[45]. We profiled both models and age-matched controls (~6-month-old, totaling 37 mouse brains), quantifying 9780 and 10,255 proteins (protein FDR < 0.01). We identified 1230 and 1564 DEPs in 3xTG and BiG, respectively (FDR < 0.05 and $|\log_2 FC| > 2$ SD, Fig. 4b and c, Supplementary Data 16, 17), including a substantial number of DEPs that are not observed in the pure amyloidosis models, 5xFAD and NLGF. While the overlap of DE proteins between 3xTG and the two amyloidosis models is relatively low, 3xTG exhibits similar trends in pathway activity changes to those in the amyloidosis models (Supplementary Fig. 5). Additionally, 3xTG shows model-specific DEPs (Fig. 4d) related to tau pathways and its downstream effects on RNA processing[63]. Similarly, the BiG mice, while sharing changes with 5xFAD, also display defective U1 snRNP splicing components similar to N40K[9], and uniquely present lipid and synaptic dysregulation that may be due to the synergy of amyloid and U1 snRNP pathways[64] (Fig. 4e, Supplementary Fig. 6).

To evaluate shared molecular changes between mouse models and human AD, we generated an upset plot highlighting overlaps in DE proteins (Supplementary Fig. 7). By summing all DEPs across the four mouse models, the overlap with human DEPs increases to 42% (275/654, Fig. 4f, Supplementary Data 14), suggesting that additional pathologies beyond amyloid plaques contribute to alterations in the mouse proteome, moving it closer to the AD spectrum. The remaining 58% of human AD DEPs show enrichment in the pathways of mitochondrial function, cell morphogenesis, lipid regulation, potentially due to reduced neuronal cell death in the mouse models and differences in response to pathological insults between mice and humans (Supplementary Data 18).

Among the 275 DEPs conserved between mouse models and human (Fig. 4f), we found that 86% are not well studied in the context of AD, with <20 AD-related publications (Supplementary Fig. 4f). We thus prioritized these proteins employing a method of order statistics[36] by integrating available 12 omics datasets from both mouse and human, which include GWAS ($n = 1$), transcriptome ($n = 2$), proteome ($n = 6$), phosphoproteome ($n = 2$), and interactome ($n = 1$) (Fig. 4g, Supplementary Data 19). As expected, well-known proteins such as APP, APOE, GFAP, TREM2, MAPT (tau), and CLU rank highly, while other proteins in the top 20 list, such as MDK, NTN1, SFRP1, OLFML3, PTPRC/CD45, SMOC1, CD180, and PTN, remain understudied (Fig. 4h). These proteins require further investigation to understand their roles in the development of AD.

Transcriptome-proteome inconsistency occurs in AD and the 5xFAD model

A transcriptome-proteome inconsistency has been reported in AD[36,37]. To explore that issue, we compared the quantitative transcriptome and proteome datasets from both human AD ($n = 10{,}781$) and 5xFAD mice ($n = 8840$) relative to their control samples, after Z-score transformation (Fig. 5a, Supplementary Data 20). We focused on 12-month-old 5xFAD mice for this comparative study, as age-matched data were available from the same breeding conditions. The transcriptome-proteome correlations were modest, with R values of 0.40 in human and 0.46 in mice (Fig. 5b, c). We identified the RNA-independent protein changes in the following steps: (i) identifying Z-score changed proteins in human AD ($n = 1121$) and in 5xFAD mice ($n = 1152$), compared to their controls; (ii) categorizing those changed proteins into four groups based on protein up-/down-regulation and RNA dependency/independency (Fig. 5d, Supplementary Data 20). Remarkably, in both species, approximately one-third of the altered proteins exhibit RNA independence (35% in humans and 36% in mice). We asked whether these RNA-independent protein changes are shared between AD and mouse models. From the 262 RNA-independent, upregulated proteins in human and 295 in mouse, there was an overlap of 31 proteins. In contrast, from the 133 RNA-independent, downregulated proteins in humans and 120 in mouse, only one overlaps (Fig. 5e). These findings suggest a partial conservation of transcriptome-proteome inconsistency of upregulated proteins in the AD mouse model.

We recognized that many of the 31 shared, upregulated proteins are present in amyloid plaques[65–69], prompting us to fully characterize the amyloidome (i.e., all the components in the amyloid plaque microenvironment) in the 5xFAD mice. We employed laser-capture microdissection (LCM) to isolate amyloid plaques and non-plaque areas from brain tissue ($n = 4$ mice) and profiled the proteome using our modified TMT-LC/LC-MS/MS pipeline, optimized for sub-microgram protein samples[70]. This approach resulted in the quantification of 5364 proteins (Fig. 5f-g, Supplementary Fig. 8, Supplementary Data 21). Quantitative comparison between the plaques and non-plaque areas identified 438 proteins enriched in plaques and 191 in non-plaque areas (FDR < 0.05 and $|\log_2 FC| > 2$ SD). Strikingly, of the 31 RNA-independent, upregulated proteins in both human AD and 5xFAD mice, 23 were detected in the amyloidome profiling, in which 17 (74%) were found among the 438 plaque-enriched proteins, while none were detected in the 191 non-plaque-enriched proteins. The results demonstrate that the formation of amyloid plaques contributes to RNA-independent protein accumulation.

Delayed protein degradation in amyloidome contributes to transcriptome-proteome inconsistency

We hypothesized that proteome-transcriptome discrepancy in AD could be due to reduced protein turnover within the amyloidome. To test this hypothesis, we employed pulsed SILAC labeling (pSILAC)[71–73] coupled with TMT to measure protein turnover rates at high throughput (Fig. 6a, Supplementary Fig. 9). The 5xFAD mice and WT littermates were fed with heavy lysine SILAC food in a time course (0, 4, 8, 16 and 32 days, with 3 replicates, totaling 30 mice), followed by brain tissue collection and TMT-LC/LC-MS/MS profiling. The kinetics of heavy lysine labeling enabled the determination of protein degradation rates, indicated by protein half-life (T_{50}). Apparent T_{50} values were calculated directly from fitting a degradation curve; to account for the recycling of heavy lysine in the mice (Supplementary Fig. 10), we

https://doi.org/10.1038/s41467-025-56853-3

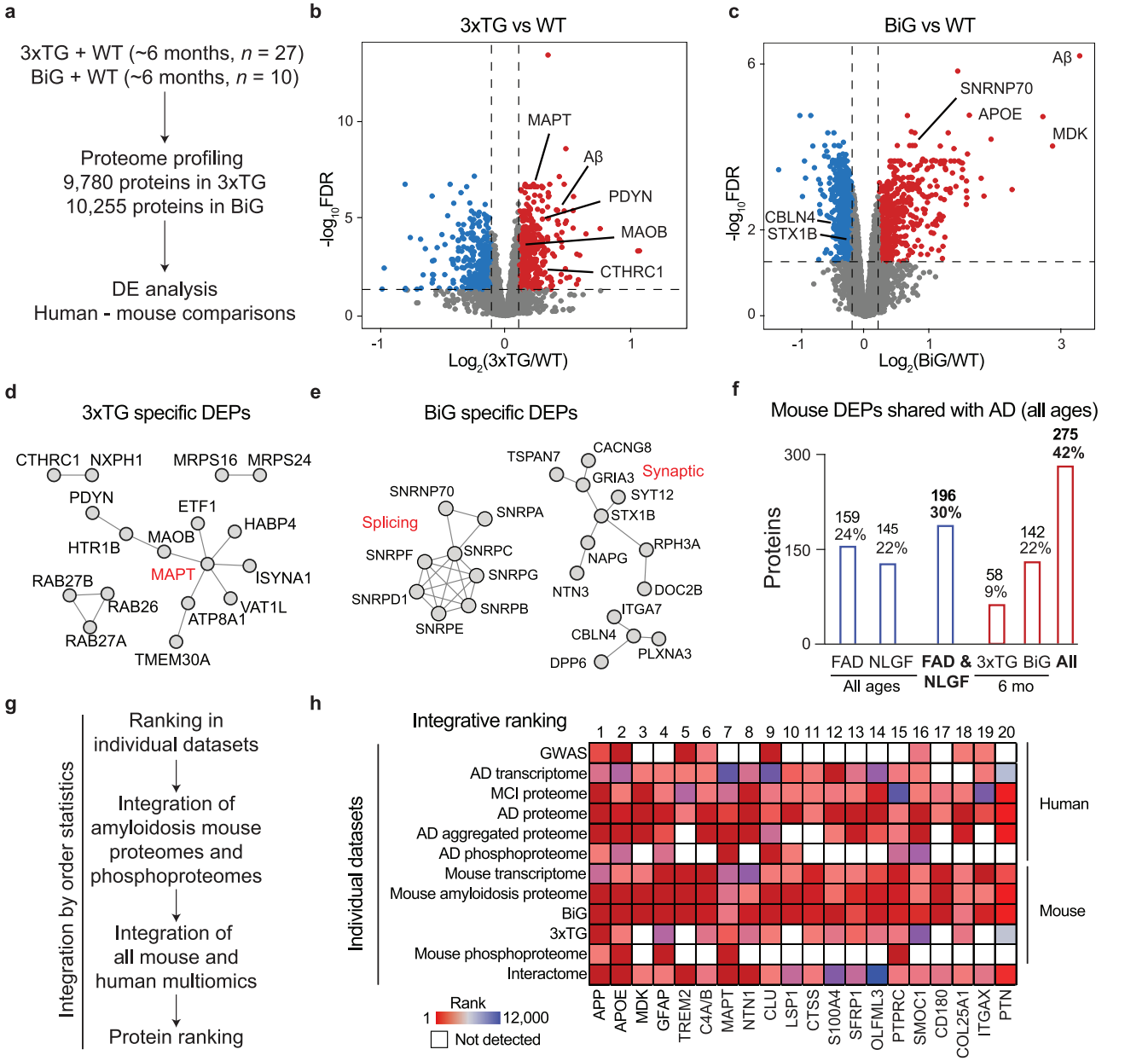

Fig. 4 | Mouse models with additional pathologies beyond amyloidosis increase the similarity to AD. a Proteomic profiling of two more mouse models that express additional AD pathologies: WT ($n = 8$) and 3xTG (Aβ and tau pathologies, $n = 19$), as well as WT ($n = 4$) and BiG (Aβ and U1 splicing pathologies, $n = 4$). All mice were ~6 months old. The proteomic data were subjected to DE analysis and comparison with human AD data. **b**, **c** Volcano plots of log_2FC and FDR in 3xTG and BiG mice, compared to WT, with DEPs highlighted in colors and cutoffs indicated by dashed lines. **d, e** Selected protein-protein interactions of significantly altered DEPs found exclusively in individual mice, such as MAPT interactome in 3xTG, and splicing/synaptic interactome in BiG. **f** Numbers of DEPs in AD mouse models that were consistently altered in AD. The percentage was calculated using a denominator of 654 AD DEPs that were detectable by MS in mice. **g** Strategy for ranking individual proteins by multi-omics using order statistics. (i) All age-dependent proteomic data from 5xFAD and NLGF were initially consolidated into two datasets for the amyloidosis proteome and phosphoproteome. (ii) These datasets were then integrated with 10 additional datasets, which include the mouse transcriptome (5xFAD), 3xTG/BiG proteomes, human genetic data from GWAS, human transcriptomes, proteomes (MCI and two independent AD studies, $n = 3$), phosphoproteome, and interactome datasets. **h** Protein integrative rankings defined by combining 12 datasets. The entire datasets were ranked based on all identified genes/proteins. Subsequently, we extracted the rankings for the AD-mouse shared proteins ($n = 275$). The top 20 proteins are displayed, with missing values represented by white boxes.

derived corrected T_{50} values using an ordinary differential equation model in the JUMPt software[73].

We quantified 12 tryptic peptides from human APP (hAPP) and mouse APP (mAPP) proteins, both present in 5xFAD (Fig. 6b, Supplementary Data 22). Two peptides were human-specific: peptide 2 in the non-Aβ region (used to quantify full-length hAPP), and peptide 10 in the Aβ region (used to quantify human Aβ (hAβ) as previously reported)[36]. The peptide spectral match (PSM) counts, a semi-quantitative index[74], for peptide 10 were significantly higher than those for peptide 2, consistent with the accumulation of Aβ in 5xFAD (Fig. 6c). Indeed, hAβ displayed a much longer half-life than hAPP (Fig. 6d–g), when analyzing apparent T_{50} (132.0 *d* for hAβ vs 40.1 *d* for hAPP) or corrected T_{50} (18.2 d for hAβ vs <0.5 d for hAPP). The results clearly indicate a significantly delayed turnover rate of hAβ relative to hAPP in the 5xFAD mice.

We then analyzed the proteome turnover for the 5xFAD and WT mice, calculating corrected T_{50} values for 8492 proteins (Fig. 7a, Supplementary Data 23). The global T_{50} distributions between 5xFAD

https://doi.org/10.1038/s41467-025-56853-3

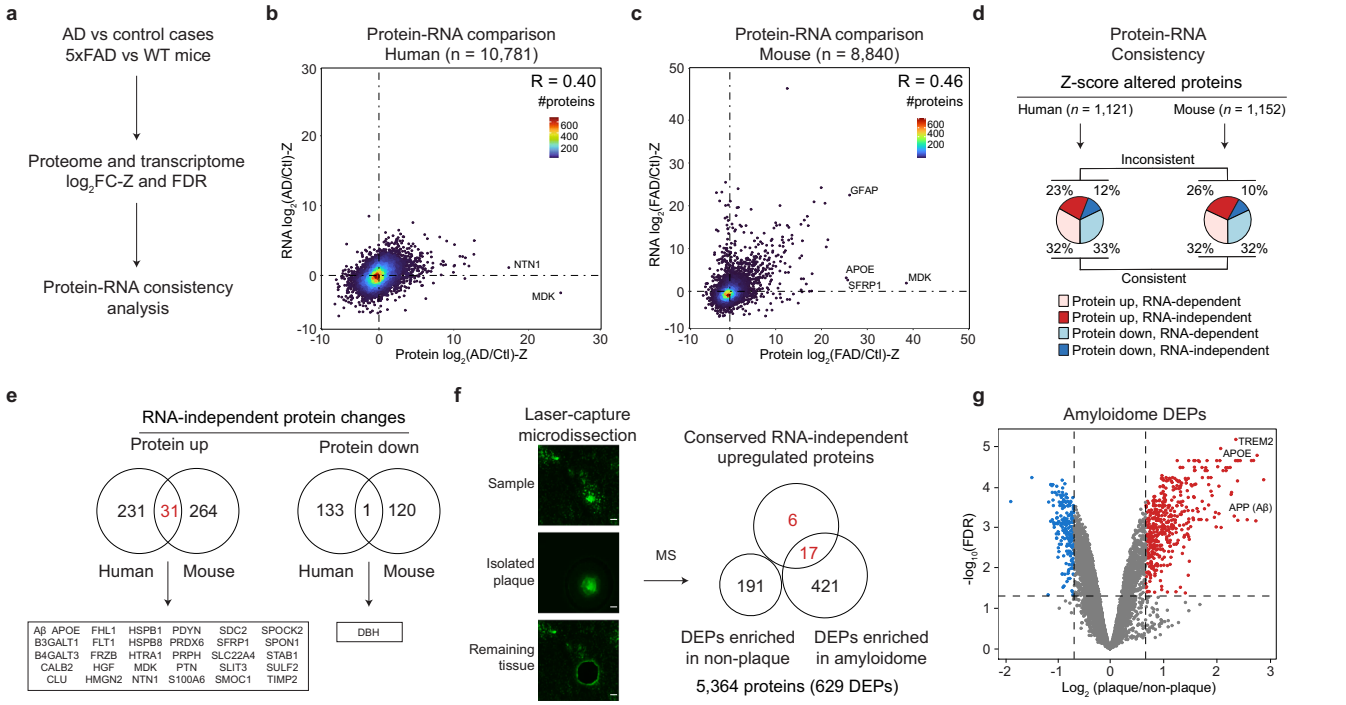

Fig. 5 | AD and the mouse model show transcriptome-proteome inconsistencies which include RNA-independent upregulated proteins enriched in the amyloidome. a Workflow for comparison of protein/RNA data to define protein-RNA consistencies. **b**, **c** Scatterplots of protein-RNA comparisons of log_2FC-Z in human ($n = 10{,}781$) and 5xFAD mice ($n = 8840$). Density is indicated by color gradients. Pearson correlation (R) values are shown. **d** Percentage of protein-RNA consistency in the population of z-score altered proteins. **e** Overlap of RNA-independent protein changes between human and mouse. **f** Workflow of LCM-MS to compare proteomes in plaque and non-plaque regions, quantifying 5364 proteins. A Venn diagram illustrated the overlap of 31 shared, RNA-independent, upregulated proteins in both humans and mice with proteins enriched in either plaque or non-plaque regions. **g** Volcano plot showing proteins enriched in plaque or non-plaque regions.

and WT were similar with average values around 4–5 d (Fig. 7b). A statistical analysis identified 84 proteins with significant changes in half-life between the two genotypes (Fig. 7c). 25% of those proteins, including DPP10 and AAK1, exhibited shorter T_{50} in 5xFAD than in WT (Fig. 7d), whereas the remaining 75% displayed longer T_{50} in 5xFAD. For example, APOE and VTN showed ΔT_{50} of 4.2 and 3.5 days, respectively (Fig. 7e).

By integrating transcriptome, proteome, amyloidome, and protein half-live data from 5xFAD, we found that 32 RNA-independent, upregulated proteins found in the amyloidome showed prolonged half-lives (Fig. 7f, Supplementary Data 24). The 32 proteins were enriched in the pathways of amyloid matrisome, autophagy/lysosome, and neurogenesis. These findings suggest that the AD transcriptome-proteome discrepancy can be attributed, at least partially, to reduced protein turnover in the amyloidome (Supplementary Fig. 11).

Discussion

A comprehensive multi-layered proteomics resource for AD mouse models

In this extensive proteomic resource, we have generated the most comprehensive AD mouse brain proteomes to date, analyzing a total of 133 mouse samples across 5 AD models (5xFAD[25,26], NLF[28], NLGF[28], 3xTG[27], and BiG[45], as well as wild type controls; Supplementary Data 2). This resource also includes phosphoproteome profiling from 36 mice (Supplementary Data 11), an in-depth amyloidome analysis from 8 mouse samples (Supplementary Data 21), and proteome turnover data from 30 mice (Supplementary Data 23). The proteome coverage is high, with most datasets surpassing 10,000 proteins, largely due to our development and implementation of a fully optimized TMT-LC/LC-MS/MS pipeline[55,70,75,76], extensive fractionation (e.g., at least 40 LC fractions per TMT batch)[46], and substantial instrument time investment (e.g., ~4 days per TMT batch). This high-quality proteomics data serves as a critical resource for comparing different mouse models, aligning mouse findings with human AD data, integrating multi-omics datasets, and identifying potential disease-related proteins.

The next-generation knock-in mouse models for amyloidosis are often considered to have higher physiological relevance and reduced overexpression artifacts compared to 5xFAD[21,23,28,77,78]. Nevertheless, our proteomic comparison highlights similarities between these models, in terms of DEPs (1382 in 5xFAD, 1142 in NLGF, Supplementary Data 7). A substantial portion (610 proteins) of DEPs overlaps between the two models, and the non-overlapping ones show similar trends in protein alterations. Furthermore, both models have a comparable number of shared DEPs with human consensus data[36,37,52,60] (159 in 5xFAD, 145 in NLGF, Supplementary Data 14). The proteomic correlation with human is also similar between the two models ($R = 0.32$ in 5xFAD, $R = 0.23$ in NLGF). Notably, NLGF mice carry the APP Arctic mutation (E693G), which produces a mutated Aβ sequence (E22G) that leads to a slightly different Aβ filament structure compared to the WT Aβ filament in 5xFAD[79,80]. This structural difference may contribute to variations in downstream molecular events. The similar proteomic patterns between the two models suggest they can be effectively used to cross-validate molecular mechanisms related to amyloidosis.

To examine the relevance of the mouse data to humans, we integrated the mouse proteomics data with publicly available human AD datasets. These human datasets were selected based on their proteomic coverage, sample diversity, and consistent reporting of key pathological markers such as amyloid and tau. Specifically, we prioritized datasets that provided high-quality differential expression data from AD brain tissues. Consistent with the understanding that mouse models cannot fully recapitulate the complexity of human AD

https://doi.org/10.1038/s41467-025-56853-3

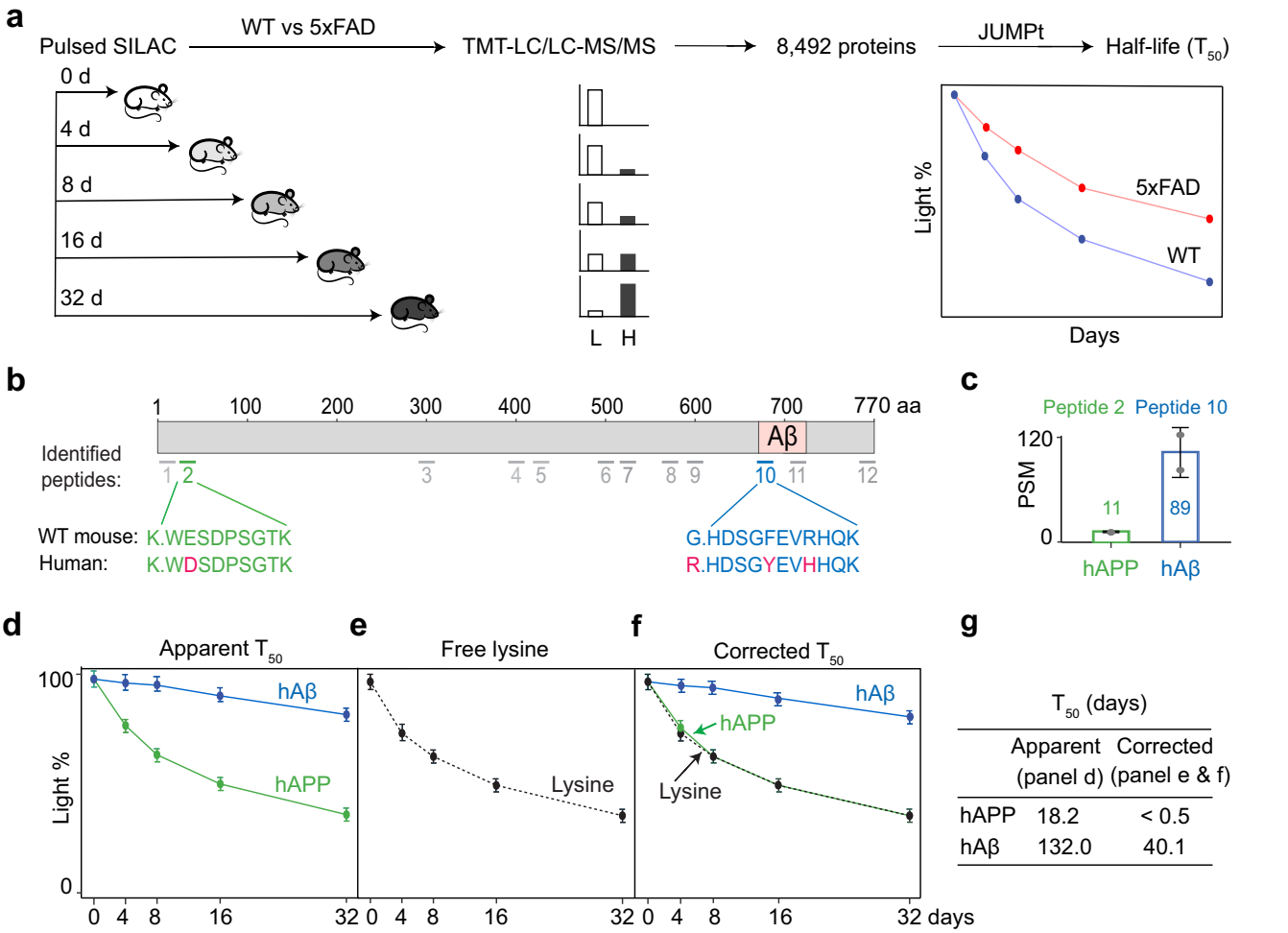

Fig. 6 | The analysis of AD mouse proteome turnover confirms distinctly different turnover rates for human APP full-length protein and Aβ peptides. **a** Whole proteome turnover analysis in 5xFAD and WT mice was performed using pulsed SILAC labeling (~9-month-old, 5 data points, 3 replicates, totaling 30 mice), TMT-LC/LC-MS/MS (2 batches), and the JUMPt program. The analysis covered a comprehensive set of 8492 unique proteins. **b** Diagram illustrating the 12 identified peptides in the human and mouse APP or Aβ regions. **c** PSM counts for the hAPP-specific peptide (peptide 2) and the hAβ surrogate peptide (peptide 10). Average PSM values are reported across 2 batches each, ±SD. **d** Apparent T_{50} values were directly determined from turnover curves for the hAPP- or hAβ-specific peptides (Average ± SD, $n = 2$). **e** The curve of free Lys amino acid (Average ± SD, $n = 2$). **f** Corrected T_{50} values were calculated based on the distance between the protein curve and free Lys curve, using the JUMPt program, which incorporates a mathematical model to account for delays caused by Lys recycling (Average ± SD, $n = 2$). **g** Summary table of hAPP and hAβ T_{50} values. The corrected T_{50} values were much smaller than the apparent T_{50} values.

events[21,23,78], our proteomic profiling of five mouse models reveals that each model shares <25% consensus DEPs of human AD data (Supplementary Data 14). Collectively, these mouse models cover ~42% of human DEPs, indicating that each model has unique characteristics and mimics different subsets of AD molecular events. For instance, tau-related pathways are observed only in 3xTG[27], whereas some splicing and synaptic defects are unique to the BiG model[45]. This proteomics resource serves as a valuable reference for investigating specific pathways using the most appropriate models.

The limitations of mouse models in replicating human AD pathology may stem from at least two factors: insufficient pathologies in mouse models and inherent species differences[81], which are not necessarily mutually exclusive. The pathogenic mechanisms demonstrated in the mice (e.g., amyloidosis) can drive only part of the AD pathologies. In human, additional pathogenic pathways induce mixed pathologies that are not observed in the mice under standard breeding conditions. For example, while the 5xFAD and NLGF models effectively mimic amyloidosis, they fail to capture broader neurodegenerative processes, such as tau pathology and mitochondrial dysfunction. Notably, these models align poorly with human MCI, instead reflecting the heavy amyloid burden characteristic of late-stage AD. While most mouse models fail to exhibit significant neuronal loss as in human, recent advancements, such as the use of human neuron xenografts in AD mice[82], promote abnormal tau phosphorylation and neuron death through necroptosis[83]. Other human-mouse chimeric models employ human microglia to better replicate AD-related responses[84]. Beyond mouse models, alternative AD models are being developed, including transgenic rats[85], human iPSCs and organoids[86–88], and primate models[89], each of which offers specific advantages. These non-mouse models may present avenues for investigating AD molecular mechanisms that are not represented in current mouse models.

Molecular insights from multi-omics integration in AD mouse models

Multi-omics integration offers a robust method to evaluate biological systems and reveal molecular insights[90], given the generally weak RNA–protein correlation, particularly in the brain which consists mainly of postmitotic, non-dividing cells[35]. In our study, both human and 5xFAD mouse brains exhibit modest RNA–protein correlations, with R values under 0.5, and approximately one-third of protein changes occur independently of RNA levels. Considering protein

https://doi.org/10.1038/s41467-025-56853-3

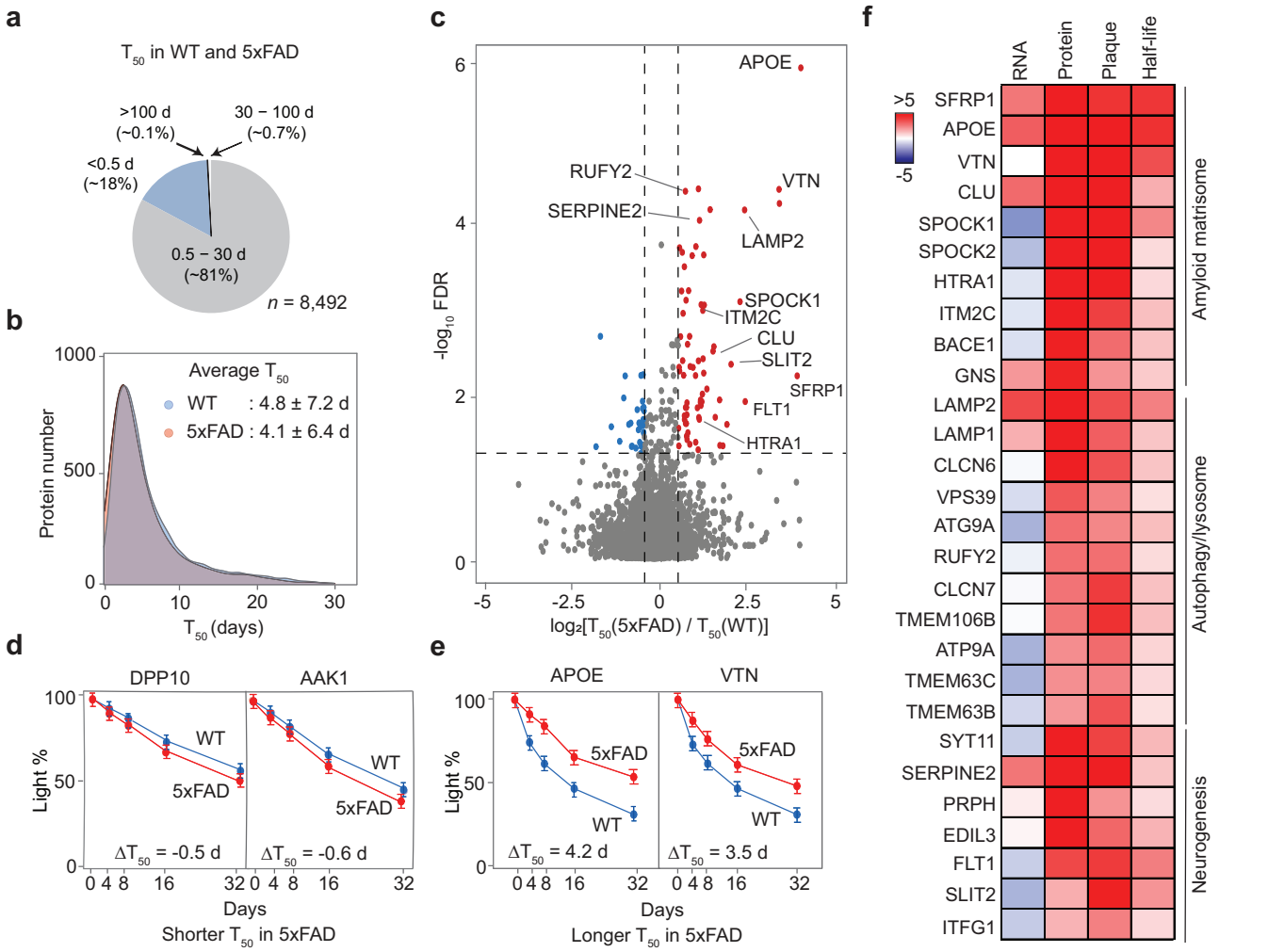

Fig. 7 | The analysis of AD mouse proteome turnover reveals slow half-lives in amyloidome proteins. a Pie chart displaying the average proportions of corrected protein T_{50} values categorized as very short (<0.5 days), intermediate (0.5–30 days), long (30–100 days), and very long (>100 days) for WT and 5xFAD mice. **b** Distribution graphs of T_{50} values in both genotypes, showing the average values and standard deviations. **c** Volcano plots of the $\log_2$ fold change and FDR for T_{50} in 5xFAD compared to WT, with proteins exhibiting changed T_{50} highlighted in colors and thresholds marked by dashed lines. **d**, **e** Examples of proteins that have shortened or extended T_{50} in 5xFAD (Average ± SD, $n = 2$ batches per genotype). **f** Heatmap illustrating how some proteins with longer T_{50} may be explained by their localization in plaques, contributing to RNA-protein discrepancies. The side bar indicates $\log_2$FC-Z values for the first three columns or $\log_2$FC values for the last column.

homeostasis is regulated by events such as modifications, localization, and turnover, we expanded our analysis to include phosphoproteome, subproteome (amyloidome with plaque localization), and protein turnover. While protein phosphorylation did not significantly account for the RNA-protein discrepancies, our multi-layered proteomic data (amyloidome and turnover) supports the hypothesis that amyloid plaque formation creates a microenvironment where as many as 32 proteins show delayed turnover, promoting their RNA-independent accumulation in the brain (Supplementary Data 24).

Amyloid plaques are dynamic and can grow to 50–100 μm in size[91]. Recent spatial omics have revealed that the Aβ core is enveloped by disease-associated microglia, activated astrocytes, and dysfunctional oligodendrocytes, positioned sequentially, implicating an active microenvironment induced by amyloid plaques (Supplementary Fig. 11)[92]. Structural analyses have shown diverse Aβ filament architectures in humans and mice[79,80], suggesting that their pathological roles are influenced by Aβ-associated proteins within the matrisome[93,94].

ApoE is a prominent protein in the amyloidome with delayed turnover. It has a well-established role in the "ApoE cascade hypothesis" supported by extensive genetic and biochemical evidence[95]. Primarily produced by astrocytes and also by microglia and neurons[96], ApoE RNA is upregulated ($\log_2$FC-Z of 3.26), but its protein change is more dramatic ($\log_2$FC-Z of 25.38). ApoE shows rapid turnover in WT mice, with a half-life of <0.5 d, but this rate slows significantly to 8.85 d in 5xFAD (Supplementary Data 23). These findings indicate that the abundant accumulation of ApoE is driven by both RNA upregulation and delayed protein turnover, possibly due to its direct interaction with Aβ in the plaque microenvironment[95].

The 32-protein list also includes several understudied proteins, such as Spock1 and Spock2, members of the Sparc proteoglycan family potentially involved in synaptic plasticity[97]; SFRP1, which may promote plaque pathology by inhibiting ADAM10 α-secretase activity in the non-amyloidogenic pathway[98]; and HTRA1, a protease potentially regulating the aggregation and clearance of amyloid proteins[99]. Genetic variations in *HTRA1* gene are linked to age-related macular degeneration[100,101]. These proteins are also found on the upregulated consensus protein list in AD brains (Supplementary Data 23), implicating a possible role in the formation of amyloid plaque microenvironment.

Interestingly, we found a number of proteins enriched in the autophagy/lysosome pathway with delayed turnover rates (Supplementary Data 24), such as Tmem106b, which has been identified as an aggregated filament protein in several neurodegenerative disorders including AD[102–104], and genetically linked to frontotemporal lobar degeneration[105]. Tmem106b accumulates in lysosomes, playing a role in lysosomal dysfunction[106]. The slow turnover of lysosomal proteins in AD mice might indicate defective autophagic degradation, possibly because lysosomes are damaged by intracellular Aβ species[107,108]. This disruption could impair cellular homeostasis, and further inhibition of lysosomal function exacerbates AD-related phenotypes, underscoring the pivotal role of lysosomal pathways in disease progression.

In summary, our study presents a comprehensive multi-layered proteomics resource, profiling five AD mouse models and providing insights into proteomic responses to AD pathologies. Through whole proteome analysis, along with phosphoproteome, amyloidome, and turnover data, the resource supports the hypothesis that amyloid plaques create a microenvironment that promotes protein accumulation. Compared with human proteomics data, this resource enables researchers to select relevant disease pathways for study in appropriate mouse models, with the potential to develop other AD models in the future. All data from this resource is freely accessible on a website (https://penglab.shinyapps.io/mouse_ad_profile/).

Methods

Mouse models in proteome analysis

The 5xFAD transgenic mice[25,26] and 3xTG mice[27] were purchased from The Jackson Laboratory (stock #034848 and #034830, respectively), while the NLF and NLGF KI mice[28] were provided by Dr. Takaomi Saido at the RIKEN Center for Brain Science. The BiG mice were generated by crossing 5xFAD with N40K transgenic mice as described previously[45]. These mice were maintained in the Animal Resource Center at St. Jude Children's Research Hospital or the University of Arizona according to the Guidelines for the Care and Use of Laboratory Animals. All animal procedures were approved by the Institutional Animal Care and Use Committee (IACUC), Protocol 542-100503. Mice were housed under a 12-h light/12-h dark cycle at 20–25 °C and 30–70% humidity. Euthanasia was performed using CO_2 inhalation at a displacement rate of 30% of the chamber volume per min, followed by confirmation of death. The brain tissues were collected at various ages, rapidly dissected, and then immediately frozen on dry ice before being stored at −80 °C. A mix of male and female mice was used (Supplementary Data 2).

Mouse SILAC labeling for protein turnover analysis

The mice were labeled using Mouse Express® L-Lysine ($^{13}C_6$, 99%) Mouse Feed (5 g per day, Cambridge Isotopes Laboratories). The mice were conditioned by providing the light SILAC food for 3 d before labeling, and then fed with the heavy SILAC food in a time course. Cortical brain tissue samples were harvested for turnover analysis. The fully labeled mice were generated as previously reported[109]. The heavy mouse chow was used to feed wild-type mice from the parental generation through to the F2 generation. Through two generations, the mouse proteins were fully labeled[109]. Only male mice were used in turnover analysis to ensure observed differences were due exclusively to differences in genotype.

Collection of amyloid plaques by LCM

LCM was performed essentially according to a previously reported method[65]. Mouse brain was embedded in OCT Compound (Jed Pella Inc., Redding, CA), sectioned at 12 μm in a cryostat and mounted on Arcturus Pen membrane glass slides (LCM0522, ThermoFisher). The sections were thawed, fixed with 75% ethanol for 1 min, stained with 1% thioflavin-S (MilliporeSigma) or X-34 (MilliporeSigma) for 1 min, washed in 75% ethanol for 1 min, dehydrated, cleared in xylene and air-dried. LCM was performed using an Arcturus XT Laser Capture Microdissection System (Arcturus, ThermoFisher) with the following settings: 495 nm excitation wavelength, 60–80 mW laser power and 1 ms duration. Although both diffuse and dense-core plaques were present in the mice, we selected X-34 stained dense-core plaques with a diameter of at least 30 μm for this study. About 500 amyloid plaques were procured from each section, while non-plaque areas were captured as a control. The captured samples were stored at −80 °C.

Protein profiling by TMT-LC/LC-MS/MS analysis

The experiments were performed according to our previously optimized protocol[110,111]. Briefly, the mouse brain samples were weighed and homogenized in lysis buffer (8 M urea, 50 mM HEPES, pH 8.5, and 0.5% sodium deoxycholate,100 μL buffer, and ~20 μL beads per 10 mg tissue) with 1 x PhosSTOP phosphatase inhibitor cocktail (Roche). ~50 μg protein from each sample was then digested in two steps by Lys-C and trypsin, with DTT reduction and iodoacetamide alkylation, followed by desalting with a C18 Ultra-Micro SpinColumn (Harvard apparatus). The desalted peptides were resuspended in 50 mM HEPES (pH 8.5) to a concentration of ~1 μg/μL, and fully labeled with TMT or TMTpro reagents. The reaction was quenched, equally pooled, and desalted for the subsequent prefractionation.

The pooled TMT samples were fractionated by offline basic reverse phase (RP) LC with an XBridge C18 column (3.5 μm particle size, 4.6 mm × 25 cm, Waters; buffer A: 10 mM ammonium formate in H_2O, pH 8.0; buffer B: 10 mM ammonium formate in 90% acetonitrile, pH 8.0). Fractions were collected in a gradient of 15–42% buffer B, and then concatenated into at least 40 samples to maintain high-resolution power. The concatenated samples were dried by SpeedVac, resuspended in 5% formic acid (FA), and analyzed by Q-Exactive HF Orbitrap MS (Thermo Fisher Scientific) in a 95 min nano-LC gradient of 15–48% buffer B (buffer A: 0.2% FA, 5% DMSO; buffer B: buffer A plus 65% acetonitrile). MS1 scan settings were 60,000 resolution, 410–1600 *m/z* scan range, 1×10^6 AGC, and 50 ms maximal ion time. MS2 settings were 20 data-dependent MS2 scans, 60,000 resolutions, starting from 120 *m/z*, 1×10^5 AGC, 120 maximal ion time, 1.0 *m/z* isolation window with 0.2 *m/z* offset, HCD, 32% specified normalized collision energy, and 15 s dynamic exclusion[70].

Phosphopeptide enrichment

The basic pH RPLC-fractionated, TMT-labeled peptides were concatenated to 10 fractions (~0.3 mg per fraction), dried, and resuspended in binding buffer (65% acetonitrile, 2% TFA, and 1 mM KH_2PO_4). TiO_2 beads (0.9 mg per sample, GL sciences) were incubated with the peptide fraction at 21 °C for 20 min. The TiO_2 beads were then washed twice with washing buffer (65% acetonitrile, 0.1% TFA) and packed into a C18 StageTip (Thermo Fisher), followed by phosphopeptide elution with the basic pH buffer (15% NH_4OH, and 40% acetonitrile). The eluates were dried and dissolved in 5% formic acid for LC-MS/MS analysis[55].

Protein identification and quantitation in the TMT analysis

The protein identification and quantification were analyzed using the JUMP software suite[47]. The MS data were searched against the protein database merged from Swiss-Prot, TrEMBL (from Uniprot), and UCSC databases (mouse: 59,423 entries). To evaluate the FDR, decoys were generated by reversing the target protein sequence[112]. Search parameters included precursor ion and product ion mass tolerance (10 ppm), maximal modification sites ($n = 3$), full trypticity, maximal missed cleavage ($n = 2$), static modification of TMT tag (+304.20715), methionine oxidation dynamic modification (+15.99491), and cysteine carbamidomethyl static modification (+57.02146) if the residue was alkylated with iodoacetamide. In the pSILAC-TMT analysis, the MS raw files were searched twice with or without Lys labeling (+6.02013). Peptide-spectrum matches (PSMs) were filtered by matching scores and mass accuracy to keep protein FDR below 1%. The peptides shared

by multiple homologous proteins were assigned by the software to the protein with the maximal PSM number, based on the rule of parsimony. The protein quantitation was performed using the TMT reporter ion based on a published method[46]. In the case of phosphoproteome profiling, we applied the JUMPl program[36] with the phosphoRS algorithm[113] to the analysis of phosphosite localization scores (Lscore, 0–100%) for each PSM, and then determine the appropriate phosphosites.

Differential expression analysis

Proteomic and phosphoproteomic analyses were performed on mouse brain samples, with protein intensities normalized by applying log2 transformation to reduce skewness and median normalization to account for variations in sample loading and global batch intensity differences. PCA, implemented with the R package *prcomp*[114], was used to evaluate the influence of covariates such as batch, sex, age, and genotype, ensuring that biological signals were not confounded by confounding variables. DE analysis was performed using a moderated *t*-test from the *MKmisc* package[115], which estimates the variance by borrowing information across all proteins or phosphopeptides, providing increased statistical power compared to traditional *t*-tests. To control for false discoveries in multiple testing, the *p* values were adjusted to FDR using the Benjamini-Hochberg procedure[116]. Proteins or phosphopeptides were designated as differentially expressed if they met two criteria: an FDR value below 0.05 and a log2 fold-change exceeding ±2 standard deviations of the dataset's global variance. The two-part threshold of FDR and fold-change is a highly stringent cutoff commonly used in high-throughput proteomics studies to minimize false discoveries. To validate this approach, a null analysis was performed by comparing half of the WT samples against the other half, applying the same threshold. No significant findings passed these criteria, confirming the appropriateness of our chosen threshold.

Pathway enrichment and protein–protein interaction network analysis

Pathway enrichment of DEPs was performed by GO enrichment analysis[50] and further analyzed by the PANTHER[117] overrepresentation test (Fisher's Exact test). Pathway enrichment specifically emphasized on GO categories relevant to neurodegenerative processes, informed by prior knowledge of AD pathogenesis. Results were filtered by FDR (below 0.01) to identify DEP-associated pathways with high confidence. DEPs within the pathways were superimposed against a custom PPI database, which combined the InWeb_IM[118], STRING[119], and BioPlex[120] databases, as detailed previously[36]. Briefly, protein modules within each cluster were determined in two steps[121]: (i) accepting PPI edges where both nodes (i.e., the connected proteins) are within the same cluster; (ii) computing a topologically overlapping matrix from the PPI network and modularizing the network into individual modules using the hybrid dynamic tree-cutting method. Modules were annotated and visualized using Cytoscape[122]. The key network hubs and interconnected modules involved in neurodegeneration were highlighted.

Differentially altered kinase activity inference by KSEA

The analysis was performed using the *KSEAapp* R package (v0.99.0) within RStudio (v4.1.2), with 122 DE phosphopeptides as input[59]. Both PhosphoSitePlus[123] and NetworKIN[124] databases were utilized to find kinase-substrate interactions and phosphosite information. Kinase substrates were extracted to derive the corresponding kinase activities for each mouse sample along with their *p* values. The *p* values for the same kinase activity across different samples were combined using Fisher's method. Kinase activities with a combined *p* value lower than 0.05 were considered significant. The log_2FC values, representing the mean log_2FC of all the kinase's substrates, were then used to generate the heatmap.

Summarization of pathway activities from individual components

We used a previously modified pathway activity inference strategy[61,62] to derive the activity of a given pathway, termed a(P), in AD and mouse model samples:

$$a(P) = \sum_{i=1}^{k} Ci \times Fi / \sqrt{k}$$

Where k represents the number of proteins in each pathway, F_i is the Log_2FC for individual proteins, and C_i denotes the functional annotation of the protein, assigned as either +1 for proteins with an activation role or -1 for proteins with an inhibitory role.

Prioritization of proteins/genes based on multi-omics datasets

We implemented a gene/protein ranking method based on order statistics for multi-omics integration[36]. This approach combines *N* distinct protein/gene ranking sets into a single comprehensive ranking. In this analysis, we utilized a total of 12 individual datasets: GWAS-identified risk loci[13–20,36], human transcriptome[125], MCI proteome[36], AD proteome datasets[36,37], AD aggregated proteome[126], AD phosphoproteome[36], 5xFAD transcriptome[36], AD amyloidosis proteome integrated from our 5xFAD and NLGF data, 3xTG proteome, BiG proteome, AD amyloidosis phosphoproteome, and interactome closeness to known AD genes by PPI network distance[36].

RNA–protein consistency analysis

To account for scale difference, proteomics and transcriptomics[36] data were converted to Z scores, generating log_2FC-Z data. RNAs and proteins with shared accessions were used for comparison. Proteins were grouped as upregulated ($Z > 2$) or downregulated ($Z < -2$). Protein-RNA consistency was determined by a ΔZ (the Z score difference between protein and RNA) absolute value larger than 2.5. However, if both RNA and protein had absolute *Z*-values larger than 4 and changed in the same direction, the pair was still considered to be consistent, regardless of Δ*Z*.

Pulse SILAC-TMT hyperplexing data processing

Following protein identification and quantification using the JUMP software suite[47], the MS raw data, and JUMP output files were further processed to remove TMT noise for accurate quantification, utilizing the JUMPsilactmt Python program (version 1.0.0). Briefly, noise levels were identified in light PSMs (the fully labeled SILAC channel) and heavy PSMs (the unlabeled channel) and subtracted from other channels (see Supplementary Fig. 9 for details). However, the TMT intensities from adjacent light/heavy PSM pairs could not be directly compared because they were produced from distinct MS scans. To address this, the JUMPsilactmt quantified the composite MS1 heavy and light ion intensities as in the SILAC quantification method[73], and used their ratio to normalize the denoised MS2 TMT reporter ion intensities in different MS scans. The normalized heavy and light TMT intensities were converted into a fraction of light (L%). Finally, quantification at the PSM level was summed to the peptide level and subsequently to the protein level. L% values were averaged across biological replicates for the JUMPt analysis.

Protein turnover rate analysis by JUMPt

Global protein half-lives were determined using JUMPt software[73] (version 1.0.0). First, we calculated the apparent T_{50} for each protein individually, using the averaged L% of the protein across time points, without accounting for in vivo Lys recycling. Next, we analyzed the corrected T50 under "Setting-2," incorporating free Lys data and L% to estimate all protein T_{50} values simultaneously using an ordinary differential equation model. It should be noted that, for proteins with very short T_{50} (<0.5 days) or very long T_{50} (>100 days), the calculation

of corrected T_{50} analysis is less reliable, though only a small fraction of proteins exhibit these extreme half-lives.

Analysis of mouse protein turnover changes

To identify statistically significant changes in T_{50} between different genotypes, the L% of each protein over the time course was analyzed by two-way ANOVA, with genotype (WT vs. 5xFAD) and labeling time (4, 8, 16, and 32 d) as variables. The ANOVA p values for genotypes were then adjusted to FDR by the Benjamini–Hochberg procedure[116]. Moreover, the ΔT_{50} for each protein was calculated as the logarithm (base 2) over the corrected T_{50} ratio between 5xFAD and WT mice. The proteins were filtered by FDR < 0.05 and $|\log_2 FC| > 2$ SD to generate the final list with altered half-lives.

Reporting summary

Further information on research design is available in the Nature Portfolio Reporting Summary linked to this article.

Data availability

RAW data results have been deposited in the PRIDE database (https://www.proteomexchange.org) and are publicly available via accession numbers PXD018590, PXD007974, PXD023395, PXD031545, PXD031732, PXD031734, PXD031735, PXD031769, PXD031830 and PXD053314 (Supplementary Data 2).

Code availability

The program of JUMPsilactmt (version 1.0.0) is publicly available from GitHub (https://github.com/abhijitju06/JUMPsilactmt-Version-0.0.1). The program of JUMPt (version 1.0.0) is available from GitHub (https://github.com/abhijitju06/JUMPt-Version-1.0.0). The program details, along with example input and output files, are provided on the respective websites.

References

1. Alzheimer's_Association. 2024 Alzheimer's disease facts and figures. *Alzheimers Dement.* **20**, 3708–3821 (2024).
2. Hyman, B. T. et al. National Institute on Aging-Alzheimer's Association guidelines for the neuropathologic assessment of Alzheimer's disease. *Alzheimers Dement.* **8**, 1–13 (2012).
3. Polanco, J. C. et al. Amyloid-beta and tau complexity - towards improved biomarkers and targeted therapies. *Nat. Rev. Neurol.* **14**, 22–39 (2018).
4. DeTure, M. A. & Dickson, D. W. The neuropathological diagnosis of Alzheimer's disease. *Mol. Neurodegener.* **14**, 32 (2019).
5. Robinson, J. L. et al. The development and convergence of co-pathologies in Alzheimer's disease. *Brain* **144**, 953–962 (2021).
6. Spillantini, M. G. et al. Alpha-synuclein in Lewy bodies. *Nature* **388**, 839–840 (1997).
7. Twohig, D. & Nielsen, H. M. α-synuclein in the pathophysiology of Alzheimer's disease. *Mol. Neurodegener.* **14**, 23 (2019).
8. Neumann, M. et al. Ubiquitinated TDP-43 in frontotemporal lobar degeneration and amyotrophic lateral sclerosis. *Science* **314**, 130–133 (2006).
9. Bai, B. et al. U1 small nuclear ribonucleoprotein complex and RNA splicing alterations in Alzheimer's disease. *Proc. Natl Acad. Sci. USA* **110**, 16562–16567 (2013).
10. Hsieh, Y. C. et al. Tau-mediated disruption of the spliceosome triggers cryptic RNA splicing and neurodegeneration in Alzheimer's disease. *Cell Rep.* **29**, 301–316 e310 (2019).
11. Tanzi, R. E. The genetics of Alzheimer disease. *Cold Spring Harb. Perspect. Med.* **2** (2012).
12. Bellenguez, C., Grenier-Boley, B. & Lambert, J. C. Genetics of Alzheimer's disease: where we are, and where we are going. *Curr. Opin. Neurobiol.* **61**, 40–48 (2020).
13. Naj, A. C. et al. Common variants at MS4A4/MS4A6E, CD2AP, CD33 and EPHA1 are associated with late-onset Alzheimer's disease. *Nat. Genet.* **43**, 436–441 (2011).
14. Lambert, J.-C. et al. Meta-analysis of 74,046 individuals identifies 11 new susceptibility loci for Alzheimer's disease. *Nat. Genet.* **45**, 1452–1458 (2013).
15. Kunkle, B. W. et al. Genetic meta-analysis of diagnosed Alzheimer's disease identifies new risk loci and implicates Abeta, tau, immunity and lipid processing. *Nat. Genet.* **51**, 414–430 (2019).
16. Jansen, I. E. et al. Genome-wide meta-analysis identifies new loci and functional pathways influencing Alzheimer's disease risk. *Nat. Genet.* **51**, 404–413 (2019).
17. Wightman, D. P. et al. A genome-wide association study with 1,126,563 individuals identifies new risk loci for Alzheimer's disease. *Nat. Genet.* **53**, 1276–1282 (2021).
18. Schwartzentruber, J. et al. Genome-wide meta-analysis, fine-mapping and integrative prioritization implicate new Alzheimer's disease risk genes. *Nat. Genet.* **53**, 392–402 (2021).
19. Bellenguez, C. et al. New insights into the genetic etiology of Alzheimer's disease and related dementias. *Nat. Genet.* **54**, 412–436 (2022).
20. Willett, J. D. S. et al. Identification of 16 novel Alzheimer's disease susceptibility loci using multi-ancestry meta-analyses of clinical Alzheimer's disease and AD-by-proxy cases from four whole genome sequencing datasets. *medRxiv* (2024).
21. Sasaguri, H. et al. APP mouse models for Alzheimer's disease preclinical studies. *EMBO J.* **36**, 2473–2487 (2017).
22. LaFerla, F. M. & Green, K. N. Animal models of Alzheimer disease. *Cold Spring Harb. Perspect. Med.* **2**, a006320 (2012).
23. Jankowsky, J. L. & Zheng, H. Practical considerations for choosing a mouse model of Alzheimer's disease. *Mol. Neurodegener.* **12**, 89 (2017).
24. Wilcock, D. M. & Lamb, B. T. The importance of continuing development of novel animal models of Alzheimer's disease and Alzheimer's disease and related dementias. *Alzheimers Dement.* **20**, 5078–5079 (2024).
25. Oakley, H. et al. Intraneuronal beta-amyloid aggregates, neurodegeneration, and neuron loss in transgenic mice with five familial Alzheimer's disease mutations: potential factors in amyloid plaque formation. *J. Neurosci.* **26**, 10129–10140 (2006).
26. Eimer, W. A. & Vassar, R. Neuron loss in the 5XFAD mouse model of Alzheimer's disease correlates with intraneuronal Abeta42 accumulation and Caspase-3 activation. *Mol. Neurodegener.* **8**, 2 (2013).
27. Oddo, S. et al. Triple-transgenic model of Alzheimer's disease with plaques and tangles: intracellular Abeta and synaptic dysfunction. *Neuron* **39**, 409–421 (2003).
28. Saito, T. et al. Single App knock-in mouse models of Alzheimer's disease. *Nat. Neurosci.* **17**, 661–663 (2014).
29. Bayés, A. & Grant, S. G. Neuroproteomics: understanding the molecular organization and complexity of the brain. *Nat. Rev. Neurosci.* **10**, 635–646 (2009).
30. Aebersold, R. & Mann, M. Mass-spectrometric exploration of proteome structure and function. *Nature* **537**, 347–355 (2016).
31. Karczewski, K. J. & Snyder, M. P. Integrative omics for health and disease. *Nat. Rev. Genet.* **19**, 299–310 (2018).
32. Forner, S. et al. Systematic phenotyping and characterization of the 5xFAD mouse model of Alzheimer's disease. *Sci. Data* **8**, 270 (2021).
33. Landel, V. et al. Temporal gene profiling of the 5XFAD transgenic mouse model highlights the importance of microglial activation in Alzheimer's disease. *Mol. Neurodegener.* **9**, 1–18 (2014).
34. Weller, A. E. et al. Single nucleus transcriptome data from Alzheimer's disease mouse models yield new insight into pathophysiology. *J. Alzheimer's. Dis.* **90**, 1233–1247 (2022).

35. Liu, Y., Beyer, A. & Aebersold, R. On the dependency of cellular protein levels on mRNA abundance. *Cell* **165**, 535–550 (2016).
36. Bai, B. et al. Deep multilayer brain proteomics identifies molecular networks in Alzheimer's disease progression. *Neuron* **105**, 975–991 (2020).
37. Johnson, E. C. B. et al. Large-scale deep multi-layer analysis of Alzheimer's disease brain reveals strong proteomic disease-related changes not observed at the RNA level. *Nat. Neurosci.* **25**, 213–225 (2022).
38. Schedin-Weiss, S. et al. Proteomics time-course study of app knock-in mice reveals novel presymptomatic Aβ 42-induced pathways to Alzheimer's disease Pathology. *J. Alzheimer's. Dis.* **75**, 321–335 (2020).
39. Savas, J. N. et al. Amyloid accumulation drives proteome-wide alterations in mouse models of Alzheimer's disease-like pathology. *Cell Rep.* **21**, 2614–2627 (2017).
40. Kim, D. K. et al. Deep proteome profiling of the hippocampus in the 5XFAD mouse model reveals biological process alterations and a novel biomarker of Alzheimer's disease. *Exp. Mol. Med.* **51**, 1–17 (2019).
41. Boeddrich, A. et al. A proteomics analysis of 5xFAD mouse brain regions reveals the lysosome-associated protein Arl8b as a candidate biomarker for Alzheimer's disease. *Genome Med.* **15**, 50 (2023).
42. Hong, I. et al. Quantitative proteomic analysis of the hippocampus in the 5XFAD mouse model at early stages of Alzheimer's disease pathology. *J. Alzheimer's. Dis.* **36**, 321–334 (2013).
43. Hark, T. J. et al. Pulse-chase proteomics of the App knockin mouse models of Alzheimer's disease reveals that synaptic dysfunction originates in presynaptic terminals. *Cell Syst.* **12**, 141–158.e149 (2021).
44. Andrews, B. et al. Multidimensional dynamics of the proteome in the neurodegenerative and aging mammalian brain. *Mol. Cell Proteom.* **21**, 100192 (2022).
45. Chen, P.-C. et al. Alzheimer's disease-associated U1 snRNP splicing dysfunction causes neuronal hyperexcitability and cognitive impairment. *Nat. Aging* **2**, 923–940 (2022).
46. Niu, M. et al. Extensive peptide fractionation and y1 ion-based interference detection method for enabling accurate quantification by isobaric labeling and mass spectrometry. *Anal. Chem.* **89**, 2956–2963 (2017).
47. Wang, X. et al. JUMP: a tag-based database search tool for peptide identification with high sensitivity and accuracy. *Mol. Cell Proteom.* **13**, 3663–3673 (2014).
48. Wang, H. et al. Systematic optimization of long gradient chromatography-mass spectrometry for deep analysis of brain proteome. *J. Proteome Res.* **14**, 829–838 (2015).
49. Bai, B. et al. Deep profiling of proteome and phosphoproteome by isobaric labeling, extensive liquid chromatography, and mass spectrometry. *Methods Enzymol.* **585**, 377–395 (2017).
50. Ashburner, M. et al. Gene ontology: tool for the unification of biology. *Nat. Genet.* **25**, 25–29 (2000).
51. Drummond, E. & Wisniewski, T. Alzheimer's disease: experimental models and reality. *Acta Neuropathol.* **133**, 155–175 (2017).
52. Bai, B. et al. Proteomic landscape of Alzheimer's disease: novel insights into pathogenesis and biomarker discovery. *Mol. Neurodegener.* **16**, 55 (2021).
53. Ballatore, C., Lee, V. M. & Trojanowski, J. Q. Tau-mediated neurodegeneration in Alzheimer's disease and related disorders. *Nat. Rev. Neurosci.* **8**, 663–672 (2007).
54. Morshed, N. et al. Quantitative phosphoproteomics uncovers dysregulated kinase networks in Alzheimer's disease. *Nat. Aging* (2021).
55. Tan, H. et al. Refined phosphopeptide enrichment by phosphate additive and the analysis of human brain phosphoproteome. *Proteomics* **15**, 500–507 (2015).
56. Solari, F. A., Dell'Aica, M., Sickmann, A. & Zahedi, R. P. Why phosphoproteomics is still a challenge. *Mol. Biosyst.* **11**, 1487–1493 (2015).
57. Franciosa, G., Locard-Paulet, M., Jensen, L. J. & Olsen, J. V. Recent advances in kinase signaling network profiling by mass spectrometry. *Curr. Opin. Chem. Biol.* **73**, 102260 (2023).
58. Dammer, E. B. et al. Quantitative phosphoproteomics of Alzheimer's disease reveals cross-talk between kinases and small heat shock proteins. *Proteomics* **15**, 508–519 (2015).
59. Wiredja, D. D., Koyuturk, M. & Chance, M. R. The KSEA App: a web-based tool for kinase activity inference from quantitative phosphoproteomics. *Bioinformatics* **33**, 3489–3491 (2017).
60. Askenazi, M. et al. Compilation of reported protein changes in the brain in Alzheimer's disease. *Nat. Commun.* **14**, 4466 (2023).
61. Lee, E., Chuang, H.-Y., Kim, J.-W., Ideker, T. & Lee, D. Inferring pathway activity toward precise disease classification. *PLoS Comput. Biol.* **4**, e1000217 (2008).
62. Wang, H. et al. Deep multiomics profiling of brain tumors identifies signaling networks downstream of cancer driver genes. *Nat. Commun.* **10**, 3718 (2019).
63. Kavanagh, T., Halder, A. & Drummond, E. Tau interactome and RNA binding proteins in neurodegenerative diseases. *Mol. Neurodegener.* **17**, 66 (2022).
64. Arendt, T. Synaptic degeneration in Alzheimer's disease. *Acta Neuropathol.* **118**, 167–179 (2009).
65. Liao, L. et al. Proteomic characterization of postmortem amyloid plaques isolated by laser capture microdissection. *J. Biol. Chem.* **279**, 37061–37068 (2004).
66. Gozal, Y. M. et al. Merger of laser capture microdissection and mass spectrometry: a window into the amyloid plaque proteome. *Methods Enzymol.* **412**, 77–93 (2006).
67. Lutz, B. M. & Peng, J. Deep profiling of the aggregated proteome in Alzheimer's disease: from pathology to disease mechanisms. *Proteomes* **6**, 46 (2018).
68. Xiong, F., Ge, W. & Ma, C. Quantitative proteomics reveals the distinct composition of amyloid plaques in Alzheimer's disease. *Alzheimers Dement* **15**, 429–440 (2019).
69. Drummond, E. et al. The amyloid plaque proteome in early-onset Alzheimer's disease and Down syndrome. *Acta Neuropathol. Commun.* **10**, 53 (2022).
70. Liu, D. et al. Deep profiling of microgram-scale proteome by tandem mass tag mass spectrometry. *J. Proteome Res.* **20**, 337–345 (2021).
71. Hinkson, I. V. & Elias, J. E. The dynamic state of protein turnover: It's about time. *Trends Cell Biol.* **21**, 293–303 (2011).
72. Ross, A. B., Langer, J. D. & Jovanovic, M. Proteome turnover in the spotlight: approaches, applications, and perspectives. *Mol. Cell Proteom.* **20**, 100016 (2021).
73. Chepyala, S. R. et al. JUMPt: comprehensive protein turnover modeling of in vivo pulse SILAC data by ordinary differential equations. *Anal. Chem.* **93**, 13495–13504 (2021).
74. Liu, H., Sadygov, R. G. & Yates, J. R. 3rd A model for random sampling and estimation of relative protein abundance in shotgun proteomics. *Anal. Chem.* **76**, 4193–4201 (2004).
75. Xu, P., Duong, D. M. & Peng, J. M. Systematical optimization of reverse-phase chromatography for shotgun proteomics. *J. Proteome Res.* **8**, 3944–3950 (2009).
76. Wang, Z. et al. 27-plex tandem mass tag mass spectrometry for profiling brain proteome in Alzheimer's disease. *Anal. Chem.* **92**, 7162–7170 (2020).

77. Xia, D. et al. Novel App knock-in mouse model shows key features of amyloid pathology and reveals profound metabolic dysregulation of microglia. *Mol. Neurodegener.* **17**, 41 (2022).
78. Zhong, M. Z., Peng, T., Duarte, M. L., Wang, M. & Cai, D. Updates on mouse models of Alzheimer's disease. *Mol. Neurodegener.* **19**, 23 (2024).
79. Yang, Y. et al. Cryo-EM structures of amyloid-beta filaments with the Arctic mutation (E22G) from human and mouse brains. *Acta Neuropathol.* **145**, 325–333 (2023).
80. Yang, Y. et al. Cryo-EM structures of amyloid-β 42 filaments from human brains. *Science* **375**, 167–172 (2022).
81. Perlman, R. L. Mouse models of human disease: An evolutionary perspective. *Evol. Med Public Health* **2016**, 170–176 (2016).
82. Espuny-Camacho, I. et al. Hallmarks of Alzheimer's disease in stem-cell-derived human neurons transplanted into mouse brain. *Neuron* **93**, 1066–1081 e1068 (2017).
83. Balusu, S. et al. MEG3 activates necroptosis in human neuron xenografts modeling Alzheimer's disease. *Science* **381**, 1176–1182 (2023).
84. Mancuso, R. et al. Xenografted human microglia display diverse transcriptomic states in response to Alzheimer's disease-related amyloid-β pathology. *Nat. Neurosci.* **27**, 886–900 (2024).
85. Do Carmo, S. & Cuello, A. C. Modeling Alzheimer's disease in transgenic rats. *Mol. Neurodegener.* **8**, 37 (2013).
86. Choi, S. H. et al. A three-dimensional human neural cell culture model of Alzheimer's disease. *Nature* **515**, 274–278 (2014).
87. Penney, J., Ralvenius, W. T. & Tsai, L. H. Modeling Alzheimer's disease with iPSC-derived brain cells. *Mol. Psychiatry* **25**, 148–167 (2020).
88. Cerneckis, J., Bu, G. & Shi, Y. Pushing the boundaries of brain organoids to study Alzheimer's disease. *Trends Mol. Med.* **29**, 659–672 (2023).
89. Jiang, Z. et al. A nonhuman primate model with Alzheimer's disease-like pathology induced by hippocampal overexpression of human tau. *Alzheimers Res. Ther.* **16**, 22 (2024).
90. Yu, J., Peng, J. & Chi, H. Systems immunology: Integrating multi-omics data to infer regulatory networks and hidden drivers of immunity. *Curr. Opin. Syst. Biol.* **15**, 19–29 (2019).
91. Walker, L. C. Abeta plaques. *Free Neuropathol.* **1** (2020).
92. Zeng, H. et al. Integrative in situ mapping of single-cell transcriptional states and tissue histopathology in a mouse model of Alzheimer's disease. *Nat. Neurosci.* **26**, 430–446 (2023).
93. Levites, Y. et al. Integrative proteomics identifies a conserved Abeta amyloid responsome, novel plaque proteins, and pathology modifiers in Alzheimer's disease. *Cell Rep. Med.* **5**, 101669 (2024).
94. Peng, J. et al. Midkine attenuates abeta fibril assembly and amyloidplaque formation. *Res. Sq.* **3**, rs-4361125 (2024).
95. Martens, Y. A. et al. ApoE Cascade Hypothesis in the pathogenesis of Alzheimer's disease and related dementias. *Neuron* **110**, 1304–1317 (2022).
96. Yamazaki, Y., Zhao, N., Caulfield, T. R., Liu, C. C. & Bu, G. Apolipoprotein E and Alzheimer disease: pathobiology and targeting strategies. *Nat. Rev. Neurol.* **15**, 501–518 (2019).
97. Vancza, L., Tatrai, P., Reszegi, A., Baghy, K. & Kovalszky, I. SPOCK1 with unexpected function. The start of a new career. *Am. J. Physiol. Cell Physiol.* **322**, C688–C693 (2022).
98. Esteve, P. et al. Elevated levels of secreted-frizzled-related-protein 1 contribute to Alzheimer's disease pathogenesis. *Nat. Neurosci.* **22**, 1258–1268 (2019).
99. Chen, S. et al. HTRA1 disaggregates alpha-synuclein amyloid fibrils and converts them into non-toxic and seeding incompetent species. *Nat. Commun.* **15**, 2436 (2024).
100. Yang, Z. et al. A variant of the HTRA1 gene increases susceptibility to age-related macular degeneration. *Science* **314**, 992–993 (2006).
101. Dewan, A. et al. HTRA1 promoter polymorphism in wet age-related macular degeneration. *Science* **314**, 989–992 (2006).
102. Schweighauser, M. et al. Age-dependent formation of TMEM106B amyloid filaments in human brains. *Nature* **605**, 310–314 (2022).
103. Jiang, Y. X. et al. Amyloid fibrils in FTLD-TDP are composed of TMEM106B and not TDP-43. *Nature* **605**, 304–309 (2022).
104. Chang, A. et al. Homotypic fibrillization of TMEM106B across diverse neurodegenerative diseases. *Cell* **185**, 1346–1355.e1315 (2022).
105. Van Deerlin, V. M. et al. Common variants at 7p21 are associated with frontotemporal lobar degeneration with TDP-43 inclusions. *Nat. Genet.* **42**, 234–239 (2010).
106. Jiao, H. S., Yuan, P. & Yu, J. T. TMEM106B aggregation in neurodegenerative diseases: linking genetics to function. *Mol. Neurodegener.* **18**, 54 (2023).
107. Lee, J.-H. et al. Faulty autolysosome acidification in Alzheimer's disease mouse models induces autophagic build-up of Aβ in neurons, yielding senile plaques. *Nat. Neurosci.* **25**, 688–701 (2022).
108. Ditaranto, K., Tekirian, T. L. & Yang, A. J. Lysosomal membrane damage in soluble Abeta-mediated cell death in Alzheimer's disease. *Neurobiol. Dis.* **8**, 19–31 (2001).
109. Dammer, E. B. et al. Polyubiquitin linkage profiles in three models of proteolytic stress suggest the etiology of Alzheimer's disease. *J. Biol. Chem.* **286**, 10457–10465 (2011).
110. Pagala, V. R. et al. Quantitative protein analysis by mass spectrometry. *Methods Mol. Biol.* **1278**, 281–305 (2015).
111. Wang, Z. et al. High-throughput and Deep-proteome Profiling by 16-plex tandem mass tag labeling coupled with two-dimensional chromatography and mass spectrometry. *J. Vis. Exp.* (2020).
112. Peng, J., Elias, J. E., Thoreen, C. C., Licklider, L. J. & Gygi, S. P. Evaluation of multidimensional chromatography coupled with tandem mass spectrometry (LC/LC-MS/MS) for large-scale protein analysis: the yeast proteome. *J. Proteome Res.* **2**, 43–50 (2003).
113. Taus, T. et al. Universal and confident phosphorylation site localization using phosphoRS. *J. Proteome Res.* **10**, 5354–5362 (2011).
114. Ihaka, R. & Gentleman, R. R: a language for data analysis and graphics. *J. Comput. Graph. Stat.* **5**, 299–314 (1996).
115. Kohl, M. Miscellaneous functions from M. Kohl [R package MKmisc version 1.9]. (2022).
116. Benjamini, Y. & Hochberg, Y. Controlling the false discovery rate: a practical and powerful approach to multiple testing. *J. Roy. Stat. Soc. B* **57**, 289–300 (1995).
117. Thomas, P. D. et al. PANTHER: Making genome-scale phylogenetics accessible to all. *Protein Sci.* **31**, 8–22 (2022).
118. Li, T. et al. A scored human protein–protein interaction network to catalyze genomic interpretation. *Nat. Methods* **14**, 61–64 (2017).
119. Mering, C. V. et al. STRING: a database of predicted functional associations between proteins. *Nucleic Acids Res.* **31**, 258–261 (2003).
120. Huttlin, E. L. et al. The BioPlex network: a systematic exploration of the human interactome. *Cell* **162**, 425–440 (2015).
121. Vanderwall, D. et al. JUMPn: a streamlined application for protein co-expression clustering and network analysis in proteomics. *J. Vis. Exp.* (2021).
122. Shannon, P. et al. Cytoscape: a software environment for integrated models of biomolecular interaction networks. *Genome Res.* **13**, 2498–2504 (2003).
123. Hornbeck, P. V. et al. PhosphoSitePlus, 2014: mutations, PTMs and recalibrations. *Nucleic Acids Res.* **43**, D512–D520 (2015).
124. Linding, R. et al. NetworKIN: a resource for exploring cellular phosphorylation networks. *Nucleic Acids Res.* **36**, D695–D699 (2008).

125. Allen, M. et al. Human whole genome genotype and transcriptome data for Alzheimer's and other neurodegenerative diseases. *Sci. Data* **3**, 160089 (2016).
126. Zaman, M. et al. Dissecting detergent-insoluble proteome in Alzheimer's disease by TMTc-corrected quantitative mass spectrometry. *Mol. Cell Proteom.* **22**, 100608 (2023).

Acknowledgements

We thank St. Jude Shared Resources and Core Facilities, including Animal Research Center, Transgenic/Gene Knockout, Proteomics and Metabolomics. We thank Takaomi C. Saido and RIKEN Brain Science Institute for providing APP^{NLF} and APP^{NLGF} mice. We thank Ines Chen for critical reading and editing. This work was partially supported by National Institutes of Health grants R01AG047928 (J.P.), R01AG053987 (J.P.), RF1AG068581 (J.P.), U54NS110435 (J.P.), U19AG069701 (J.P.), RF1AG064909 (G.Y. and J.P.), and the ALSAC foundation.

Author contributions

J.P., X.H., G.Y., and Y.L. conceived this project. J.M.Y., X.H., K.Yang, D.L., M.Z., Z.W., K.Yu, D.G.L., D.V., M.N., H.S, B.X., P.-C.C, Y.J., X.Z., Z.W., B.V., Q.H., A.T., P.T.R., and R.C. performed the experiments. J.M.Y., X.H., A.D., K.Yang, H.K.S., S.R.C., Y.F., Y.L., Z.-F.Y., X.W., S.P., G.Y., Y.L., and J.P. analyzed the data. J.M.Y., X.H., A.D., and J.P. wrote the manuscript.

Competing interests

The authors declare no competing interests.

Additional information

Supplementary information The online version contains supplementary material available at https://doi.org/10.1038/s41467-025-56853-3.

Correspondence and requests for materials should be addressed to Junmin Peng.

Peer review information *Nature Communications* thanks Seth Grant, Sung-Ung Kang and the other, anonymous, reviewers for their contribution to the peer review of this work. A peer review file is available.